Journal of Computational Physics 513 (2024) 113149

Contents lists available at ScienceDirect

Journal of Computational Physics

journal homepage: www.elsevier.com/locate/jcp

Physically consistent modelling of surface tension forces in the Volume-of-Fluid method for three or more phases

Élfego Ruiz-Gutiérrez [a,*], Josef Hasslberger [b], Markus Klein [b], Kenny Dalgarno [a], Nilanjan Chakraborty [a]

[a] Newcastle University, School of Engineering, Claremont Road, Newcastle upon Tyne, NE1 7RU, UK
[b] University of the Bundeswehr Munich, Department of Aerospace Engineering, Werner-Heisenberg-Weg 39, 85577 Neubiberg, Germany

ARTICLE INFO

Keywords:
Multiphase flows
Volume-of-Fluid
Surface tension forces
Conservative schemes
Force balance

ABSTRACT

Multiphase numerical simulations have become a widely sought methodology for modelling capillary flows due to their scientific relevance and multiple industrial applications. Much progress has been achieved using different approaches, and the volume of fluid is one of the most popular methods widely used for modelling two or more phases due to its simplicity, accuracy and robustness. However, when prescribing the forces emerging from three or more fluid-fluid interfaces, the force balance is not guaranteed and can lead to spurious self-propulsion. Here, a new approach to account for the surface tension forces for multiphase flows with a correct force balance is proposed. The newly proposed method is successfully validated for a wide range of tests, including contact angles for the fluid-fluid and fluid-solid triple line. Additionally, complete spreading phenomena of fluid on fluid and fluid on solid have been found to emerge naturally from the newly proposed surface tension force model. Finally, simulation results are compared against experiments of lubricant-impregnated surfaces to demonstrate the practical applicability of the newly proposed method.

1. Introduction

The modelling of fluid systems that consist of three or more phases is important for industrial applications, such as phase separation in pyrometallurgy and multicomponent alloys [1–4], oil separation in wastewater [5–7], atomisation and digital microfluidics for pharmaceutical applications [8–10]. Additionally, multiphase flows involving three or more phases are relevant from the point of view of fundamental physics, for example, the chemistry and adhesion of thin films over surfaces [11], including lubricant-impregnated surfaces [12–14]. Therefore, modelling multiphase fluids of more than two phases has become highly relevant.

Several methods have addressed the modelling of flows of three or more phases. One of the popular choices is the phase-field method. Broadly, this numerical method is based on a free energy functional of the phase fields from which the thermodynamic properties of the fluid are prescribed [15–23]. Therefore, the physical properties of the system, such as chemical potential, pressure, surface tension, disjoining pressure and solid surface wettability, are derived. However, the unrealistic thickness of the interfaces and the large compressibility of the liquids might become cumbersome and expensive to avoid when simulating liquids far from the critical point.

* Corresponding author.
E-mail address: elfego.ruiz-gutierrez@newcastle.ac.uk (É. Ruiz-Gutiérrez).

https://doi.org/10.1016/j.jcp.2024.113149
Received 26 May 2023; Received in revised form 24 May 2024; Accepted 25 May 2024

Available online 31 May 2024

Another common approach is the level-set method [24–27]. In this method, the interface is defined by the contour of a marker function, which evolves by the advection of the flow. Level-set methods are usually valid for incompressible flows and allow for highly accurate calculation of the interfacial properties, such as the mean curvature, with high accuracy. Nonetheless, the marker function must be "reinitialised" to restore the smoothness of the interface after advection, which may cause poor volume conservation [28,29].

Perhaps the most popular alternative approach to multiphase flows is the Volume-of-Fluid (VoF) method, which similarly uses a field to identify each phase, the volume fraction. Most VoF methods ensure mass conservation while retaining a sharp interface, whilst they can naturally handle topological changes of the interfaces [30]. The challenge in this method is reconstructing the interface during its advection for an accurate calculation of the surface tension forces [20,31]. Much progress has been achieved in this endeavour, particularly in the correct representation of the triple line, the region in space where three interfaces meet [32–35].

A popular approach to more than two-phase flows in the VoF method was pioneered by Bonhome et al. [36] and followed by Personnetaz et al. [37] and Bublik and Einarsrud [38]. Their surface tension model consists of superimposing the pairwise surface tension and curvatures of each interface. It will be demonstrated in the following sections that the total momentum is not always guaranteed to be conserved, thus leading to unphysical propulsion.

At the same time, several multiphase models have been derived for phase-field methods. These methods are based on a free energy functional, which allows thermodynamic consistency in deriving the chemical potential of each component and total pressure. However, choosing a realistic free energy functional might present challenges, such as the appearance of an interstitial third phase between two phases [18].

One way of avoiding the interstitial phase is to add an energy penalty term that peaks in the presence of all phases [17,39–41]. Additionally, the surface tension coefficients can be expressed in terms of the spreading parameters, Γ_i, such that $\Gamma_i := (\gamma_{ij} + \gamma_{ik} - \gamma_{jk})/2$, $i \neq j \neq k$. This approach is very convenient, for ternary fluids, as the number of phases equals the number of pairwise interface combinations.

The ternary fluid approach has been adapted successfully into the VoF method [42]. In this case, the surface tension force, $\boldsymbol{f}_{\mathrm{st}}$, can be rewritten as $\boldsymbol{f}_{\mathrm{st}} = \sum_{i=1}^{3} \Gamma_i \kappa_i \hat{\boldsymbol{n}}_i \delta(S_i)$ where κ_i is the curvature, $\hat{\boldsymbol{n}}_i$ is the unit normal vector, and $\delta(S_i)$ is a surface density function of the boundary of the i-th phase given by the manifold $\{\boldsymbol{x} | S_i(\boldsymbol{x}) = 0\}$. This method is conceptually different from the approach by Bonhome et al. [36] and has the advantage that it is computationally more efficient. Unfortunately, the generalisation is not evident to an arbitrary number of phases, as the number of pairwise interfaces increases faster than the number of phases after three. Therefore, the relation between the spreading parameters and the surface tension combinations becomes undetermined for more than three phases.

Here, a new method for prescribing the surface tension forces consistent with the laws of motion is proposed. Our model has been tested for the algebraic VoF with interface compression in which the forces can be expressed in terms of gradients of the volume fraction fields. The new formulation has been implemented in the open-source code, OpenFOAM, since it can be extended for additional physics with some simplicity and is well-validated and accepted in the Computational Fluid Dynamics community [43,44]. Moreover, the surface tension force scheme presented in this work is not particular to the code implementation, as it does not require functions or subroutines specific to the code. Furthermore, it can be generalised and applied to many other methods.

2. Multiphase model

In the Volume-of-Fluid (VoF) method, phase i is identified by a volume fraction field, $\alpha_i(\boldsymbol{x}) \in [0, 1]$; $\alpha_i = 1$ corresponds to the bulk of phase i, whereas $\alpha_i = 0$ corresponds to the absence of that phase. The coexistence of M phases imposes the constraint

$$\sum_{i=1}^{M} \alpha_i(\boldsymbol{x}) = 1 \quad \forall\, \boldsymbol{x} \in \Omega, \tag{1}$$

where Ω denotes the region where the multiphase fluid mixture is defined. The volume-fractions are governed by the conservation equations

$$\partial_t \alpha_i + \boldsymbol{\nabla} \cdot (\alpha_i \boldsymbol{u}) = 0, \qquad \text{for } i = 1, 2, ..., M \tag{2}$$

where t is the time variable, R and $\boldsymbol{u}$ is the velocity field of the fluid mixture. The velocity field is subject to the incompressible Navier-Stokes equation,

$$\partial_t(\rho \boldsymbol{u}) + \boldsymbol{\nabla} \cdot (\rho \boldsymbol{u} \otimes \boldsymbol{u}) = -\boldsymbol{\nabla} p + \boldsymbol{\nabla} \cdot [\rho \nu (\boldsymbol{\nabla} \boldsymbol{u} + \boldsymbol{\nabla} \boldsymbol{u}^T)] + \boldsymbol{f}_{\mathrm{st}}, \tag{3}$$

where ρ is the density, p is the pressure, ν is the kinematic viscosity and $\boldsymbol{f}_{\mathrm{st}}$ are the surface tension forces.

To formulate the model for the surface tension forces, three requirements are imposed as illustrated in Fig. 1. Considering the stress-based formalism detailed in Appendix A, expressing the surface tension forces as

$$\boldsymbol{f}_{\mathrm{st}} = -\boldsymbol{\nabla} \cdot \left(\sum_{i=1}^{M} \sum_{k=i+1}^{M} \boldsymbol{\Pi}_{ik} \right) \tag{4}$$

is proposed in this work, where the tensor $\boldsymbol{\Pi}_{ik}$ is defined as

$$\boldsymbol{\Pi}_{ik} := -\gamma_{ik} \left(\mathbf{I} - \hat{\boldsymbol{n}}_{ik} \otimes \hat{\boldsymbol{n}}_{ik} \right) \delta_{ik}^{(S)}, \tag{5}$$

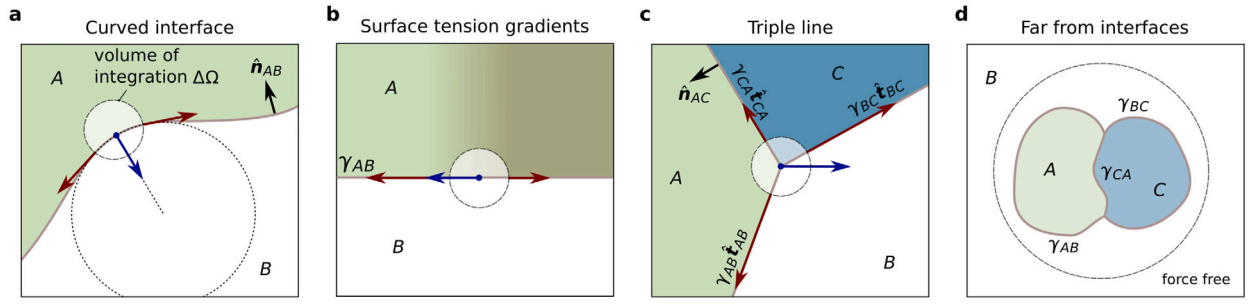

Fig. 1. Illustration of the surface tension forces acting on a multiphase fluid. A volume of integration surrounding some area of interest is highlighted to show the forces arising from surface tension. (a) For a gently curved interface, the change in tangential stresses (red arrows) produces a force proportional to the curvature of the interface (blue arrow). (b) When the surface tension varies along the interface, the resulting force has a tangential component to the surface. (c) The forces arising at the intersection of three phases, i.e., the triple line. (d) Far from interfaces, the resulting surface tension force should vanish, ensuring that momentum is conserved. (For interpretation of the colours in the figure(s), the reader is referred to the web version of this article.)

where γ_{ik} corresponds to the surface tension of the ik-interface. In Eq. (5), $\hat{\boldsymbol{n}}_{ik}$ corresponds to the unitary normal vector exclusively defined at the ik-interface and pointing at the bulk of phase i. $\delta_{ik}^{(S)} = \delta_{ik}^{(S)}(\boldsymbol{x})$ is a surface density function [45] which, ideally, tends to the Dirac delta function for an infinitely sharp interface, $\delta_{ik}^{(S)} \to \delta(S_{ik}(\boldsymbol{x}))$ for $S_{ik} : \mathbb{R}^3 \to \mathbb{R}$ such that $S_{ik}(\boldsymbol{x}) = 0$ for all points on the ik-interface. This implies that $\boldsymbol{\Pi}_{ik}$ corresponds to the stresses exerted by the surface tension of the ik-interface. Additionally, the term $\mathbf{I} - \hat{\boldsymbol{n}}_{ik} \otimes \hat{\boldsymbol{n}}_{ik} = \hat{\boldsymbol{t}}_{ik}^{(1)} \otimes \hat{\boldsymbol{t}}_{ik}^{(1)} + \hat{\boldsymbol{t}}_{ik}^{(2)} \otimes \hat{\boldsymbol{t}}_{ik}^{(2)}$ is a projector onto the tangential components of the interface, where $\hat{\boldsymbol{t}}_{ik}^{(1)}$ and $\hat{\boldsymbol{t}}_{ik}^{(2)}$ are unitary vectors perpendicular to each other and to $\hat{\boldsymbol{n}}_{ik}$, therefore, tangential to the interface ik. Note the parity of the vector, $\hat{\boldsymbol{n}}_{ik} = -\hat{\boldsymbol{n}}_{ki}$ and the symmetry of $\gamma_{ik} = \gamma_{ki}$ and $\delta_{ik}^{(S)} = \delta_{ki}^{(S)}$, which implies $\boldsymbol{\Pi}_{ik} = \boldsymbol{\Pi}_{ki}$. Consequently, it suffices to range $i = 1, 2, ..., M$ and $k = i+1, i+2, ..., M$ to avoid repeating terms in the sum of Eq. (4).

The case of a gently curved interface is examined first. For this configuration, the well-known scheme of a two-phase system is recovered. This can be demonstrated by considering the case shown in Fig. 1(a); when performing an integration over a finite but arbitrary volume, $\Delta\Omega$, enclosing the AB interface, the surface tension force results in

$$\int_{\Delta\Omega} \boldsymbol{f}_{\mathrm{st}}\, \mathrm{d}V = -\int_{\partial\Delta\Omega} \boldsymbol{\Pi}_{AB} \cdot \mathrm{d}\boldsymbol{\sigma} = \oint_{C} \gamma_{AB}\, \hat{\boldsymbol{t}}_{AB}^{(\ell)}\, \mathrm{d}\ell, \tag{6}$$

where $\mathrm{d}\boldsymbol{\sigma}$ is the infinitesimal surface vector. For the first equality the divergence theorem has been used and the only surviving term in the sum corresponds to $i = A$ and $k = B$. On the second equality in Eq. (6), $C = \partial(\Delta\Omega \cap \{\boldsymbol{x} | S_{AB}(\boldsymbol{x}) = 0\})$ is defined to be the closed circuit on the AB-interface, $\mathrm{d}\ell$ is an infinitesimal displacement around the circuit, and $\hat{\boldsymbol{t}}_{ik}^{(\ell)}$ is the tangent vector to the AB interface which is also perpendicular to C. This expression of the surface tension forces for two-phase flows is sometimes preferred as it avoids calculating an additional numerical derivative [28]. However, it can be shown that, as the volume becomes vanishingly small, using the Frenet-Serret identities [46], the force tends to be proportional to the curvature of the interface and oriented in the normal direction,

$$\boldsymbol{f}_{\mathrm{st}} \to -\gamma_{AB} \kappa_{AB} \hat{\boldsymbol{n}}_{AB} \delta_{AB}^{(S)} \qquad \text{for a single interface,} \tag{7}$$

where $\kappa_{AB} := \boldsymbol{\nabla} \cdot \hat{\boldsymbol{n}}_{AB}$ corresponds to the mean curvature of the AB-interface. The force contribution from Eq. (7) results in the well-known Laplace's pressure jump across an interface, that is,

$$\Delta_{AB} p = \gamma_{AB} \kappa_{AB}, \tag{8}$$

where $\Delta_{AB} p = \lim_{\epsilon \to 0} [p(\boldsymbol{x}_{AB} + \hat{\boldsymbol{n}}_{AB}\epsilon) - p(\boldsymbol{x}_{AB} - \hat{\boldsymbol{n}}_{AB}\epsilon)]$ represents the discontinuity at the point $\boldsymbol{x}_{AB}$ on the interface.

Moreover, the surface tension of the AB interface can vary with position, i.e., $\gamma_{AB} = \gamma_{AB}(\boldsymbol{x}_{AB})$, $\boldsymbol{x}_{AB} \in \{\boldsymbol{x} | S_{AB}(\boldsymbol{x}) = 0\}$, as shown in Fig. 1(b). This phenomenon can occur, for instance, due to the presence of surfactants or local temperature variations [47]. The total force at the volume of integration on a flat surface follows from Eq. (6); however, in this case, it results in a force tangential to the surface. As the circuit, C, is collapsed into a point, the surface tension force reads,

$$\boldsymbol{f}_{\mathrm{st}} \to \delta_{AB}^{(S)} \boldsymbol{\nabla}_S \gamma_{AB} \tag{9}$$

in the limit of $\ell \to 0$, where $\boldsymbol{\nabla}_S$ corresponds to the gradient operator on the manifold S.

As depicted in Fig. 1(c), at the triple line, the volume integral of the surface tension force results in

$$\int_{\Delta\Omega} \boldsymbol{f}_{\mathrm{st}}\, \mathrm{d}V = \sum_{ik}{}' \gamma_{ik} \hat{\boldsymbol{t}}_{ik} \ell, \tag{10}$$

where $\sum'$ implies the sum of all the interfaces captured within the volume of integration, $\hat{\boldsymbol{t}}_{ik}$ is the tangential vector to the ik-interface pointing out of the integration volume, and ℓ is the length of the triple line enclosed by integral. In equilibrium, the forces at the triple point must balance, thus satisfying Neumann's construction [47,48],

$$\sum_{ik}^{\prime} \gamma_{ik} \hat{\boldsymbol{t}}_{ik} = \boldsymbol{0}. \tag{11}$$

Lastly, carrying out a volume integration such that the boundary does not intersect any interfaces should result in a zero total surface tension force. This implies that the total momentum of a multiphase capillary system, such as the one illustrated in Fig. 1(d), is constant. Note that deriving the surface tension forces from the divergence on a tensor field that vanishes away from the interfaces ensures the balance of forces and thus avoids self-propulsion.

3. Numerical method

For numerical purposes, $\delta_{ik}^{(S)}$ is required to span over a few mesh nodes. Following Pope [49], the surface density function is constructed from the gradient of a scalar field that ranges from zero to one, such as the volume fraction. Then,

$$\delta_{ik}^{(S)} = |\boldsymbol{m}_{ik}|, \tag{12}$$

is defined, where

$$\boldsymbol{m}_{ik} := \alpha_k \boldsymbol{\nabla} \alpha_i - \alpha_i \boldsymbol{\nabla} \alpha_k. \tag{13}$$

On the one hand, far from any other phase on the ik-interface, the expression $\alpha_i + \alpha_k = 1$ holds, and thus, $\boldsymbol{m}_{ik}$ becomes $\boldsymbol{\nabla}\alpha_i = -\boldsymbol{\nabla}\alpha_k$. On the other hand, $\boldsymbol{m}_{ik}$ becomes zero far from the ik-interface, which includes sections of the i-interface that are not shared by the k-interface. A more detailed exposition of how the field $|\boldsymbol{m}_{ik}|$, with $\boldsymbol{m}_{ik}$ as defined in Eq. (13), represents the surface density function, $\delta_{ik}^{(S)}$, can be found in Appendix B. Furthermore, the vector field $\boldsymbol{m}_{ik}$ is used to define the unit normal vector to the ik-interface, that is,

$$\hat{\boldsymbol{n}}_{ik} := \frac{\boldsymbol{m}_{ik}}{|\boldsymbol{m}_{ik}|}. \tag{14}$$

The substitution of Eqs. (12) and (14) into Eq. (5) following Eq. (4) results in

$$\boldsymbol{f}_{\mathrm{st}} = \sum_{i=1}^{M} \sum_{k=i+1}^{M} \left[-\gamma_{ik}\, \kappa_{ik}\, \boldsymbol{m}_{ik} + |\boldsymbol{m}_{ik}| \left(\mathbf{I} - \hat{\boldsymbol{n}}_{ik} \otimes \hat{\boldsymbol{n}}_{ik} \right) \boldsymbol{\nabla} \gamma_{ik} + 2\gamma_{ik} \left(\boldsymbol{\nabla}\alpha_i \times \boldsymbol{\nabla}\alpha_k \right) \times \hat{\boldsymbol{n}}_{ik} \right]. \tag{15}$$

The first term in Eq. (15) corresponds to the contribution due to the curvature of the interface and is identified as the term from Eq. (7) smeared over a finite volume. This term is commonly implemented in many models of multiphase flows. The following term accounts for local variations of the surface tension that occur over the interface, thus resulting in the tangential forces acting on the interface [50]. However, we will restrict ourselves to constant surface tensions, γ_{ik}, in all interfaces; therefore, this phenomenon will not be addressed in this work.

The last term in Eq. (15), localises the forces at the triple line, where each component in the sum is tangent to the ik-interface. As shown in Appendix B, the term $2\boldsymbol{\nabla}\alpha_i \times \boldsymbol{\nabla}\alpha_k$ from Eq. (15) corresponds to a vector field that is tangent to the triple line and its magnitude conforms the line density function, $\delta_{ik}^{(L)}$, of the perimeter of the ik interface. Therefore, this vector can be expressed as

$$2\boldsymbol{\nabla}\alpha_i \times \boldsymbol{\nabla}\alpha_k = \hat{\boldsymbol{b}}_{ik} \delta_{ik}^{(L)}, \tag{16}$$

where $\hat{\boldsymbol{b}}_{ik}$ is the unit tangent vector to the perimeter of the ik-interface in the counter-clockwise direction and orthogonal to $\hat{\boldsymbol{n}}_{ik}$. Moreover, its cross product with $\hat{\boldsymbol{n}}_{ik}$ results in the unitary vector that points into the ik-interface, i.e., $\hat{\boldsymbol{t}}_{ik} = \hat{\boldsymbol{b}}_{ik} \times \hat{\boldsymbol{n}}_{ik}$. Therefore, the last term in Eq. (15) corresponds to a vector field pointing inwards to the ik-interface and that is localised at the perimeter of the interface.

For numerical purposes, a term is added to Eq. (2) to maintain the sharpness of the interface. This approach is commonly referred to as the algebraic VoF, which reads,

$$\partial_t \alpha_i + \boldsymbol{\nabla} \cdot (\alpha_i \boldsymbol{u}) = \boldsymbol{\nabla} \cdot \left(\alpha_i (1 - \alpha_i) \boldsymbol{u}_r \right), \tag{17}$$

where $\boldsymbol{u}_r$ in the right-hand side is defined as

$$\boldsymbol{u}_r := -c_\alpha\, |\boldsymbol{u}|\, \frac{\boldsymbol{\nabla}\alpha_i}{|\boldsymbol{\nabla}\alpha_i|}, \tag{18}$$

and c_α is known as the interface compression coefficient. The velocity, $\boldsymbol{u}_r$, in Eq. (18) produces a counter-gradient current that aims to cancel the numerical diffusivity of the interface from the advection scheme [51]. Without loss of generality, at every time step, Eq. (17) is iterated for the first $M - 1$ phases, then, the remaining volume fraction field, α_M, is calculated by means of Eq. (1).

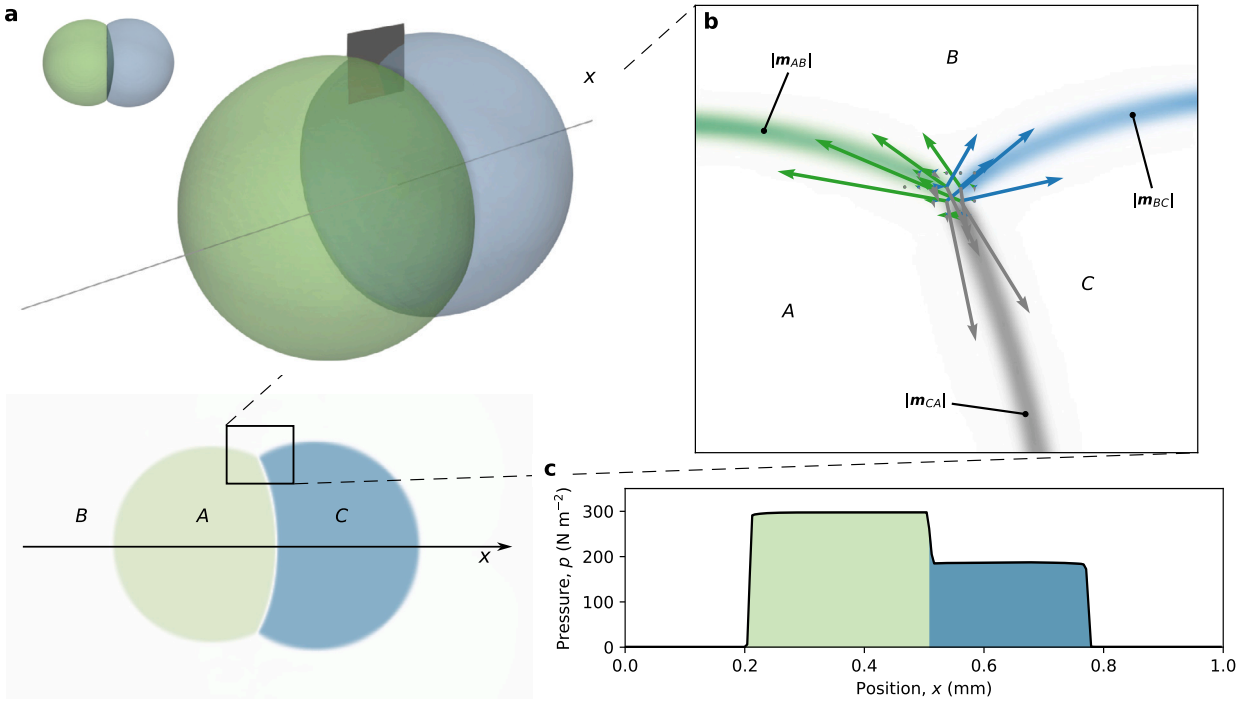

Fig. 2. Numerical simulation showing the surface tension forces of a three-phase flow of a suspended binary droplet in equilibrium. (a) An example of a binary droplet of phases A and C suspended in a third phase, B. (b) A close up to the triple line region, where the shaded regions are showing the intensity of the smeared field $|\boldsymbol{m}_{ik}|$ indicating the position of the three interfaces. The arrows correspond to the tangential forces calculated using the second term in Eq. (15). (c) The equilibrium pressure profile along the axis of symmetry. The shaded regions show the location of each of the phases. The simulation dimensions, L_i, and mesh resolution, N_i are $L_x \times L_y \times L_z = 1\,\text{mm}^3$ and $N_x \times N_y \times N_z = 160^3$, respectively. Periodic boundary conditions are set in all directions. The system relaxes for 20 ms. The surface tensions are γ_{AB}, γ_{BC} and γ_{CA} are 40, 50 and 60 mN m^{-1}, respectively. Further technical specifications are described in Sec. 4. (Colour online)

It is worth emphasising that the formulation for the surface tension forces is not restricted to the algebraic VoF since Eqs. (4) or (15) are valid independently of the scheme employed to advect the interface.

Note that for a two-phase system, Eq. (15) reduces to the expected result since the second term vanishes because $\boldsymbol{\nabla}\alpha_i = -\boldsymbol{\nabla}\alpha_k$. In a two-phase flow, the sum in Eq. (15) contains only one term, where $i = 1$ and $k = 2$. Therefore, the cross-product in the second term vanishes.

Fig. 2 illustrates the results of a simulation of a suspended binary droplet that has reached equilibrium. The figure shows the different contributions of the surface tension forces. As the system relaxes, the interfaces form spherical sections, as shown in Fig. 2(a) and the angle between the interfaces converges to equilibrium.

Fig. 2(b) shows the surface density functions $|\boldsymbol{m}_{AB}|$, $|\boldsymbol{m}_{BC}|$ and $|\boldsymbol{m}_{CA}|$ and their intersection at the triple line. Additionally, the contribution of the last term in Eq. (15) from each interface converging at the triple line can be observed. This is the contribution of each of the forces at the triple line, pointing in the direction of their respective interfaces away from the triple line, and the result is a zero-sum force, consistent with Eq. (11). Lastly, Fig. 2(c) shows the pressure profile along the symmetry axis for the binary droplet configuration. The sequence of pressure jumps at each interface can be observed, which is a direct consequence of the force distribution due to the curvature of the interface.

The modelling of the boundary conditions for solid surfaces is now addressed. Two boundary conditions for partially wetting fluids on solids were implemented and will be tested in Section 4. The first of these, which shall be called the thermodynamic approach, consists of emulating the solid as an additional phase, α_{solid}. Therefore, $\alpha_{\text{solid}} = 1$ only at the solid boundary and $\alpha_{\text{solid}} = 0$ everywhere else. Then, the spreading of some phase i versus another k can be specified by setting the surface tensions, $\gamma_{i\,\text{solid}}$ and $\gamma_{k\,\text{solid}}$, respectively, for a given γ_{ik}. Therefore, one is free to choose the values for $\gamma_{k\,\text{solid}}$ and $\gamma_{i\,\text{solid}}$ to prescribe the contact angle of the ik-interface.

The second method, which shall be deemed the geometric approach, consists of redirecting the vector $\boldsymbol{m}_{ik}$ to satisfy the prescribed contact angle at each interface that reaches the solid boundary. Since this acts at each interface independently, the algorithm can be imported from two-phase modelling. Following the work of Ding and Spelt [52], the vector

$$\boldsymbol{m}_{ik} \rightarrow \boldsymbol{m}_{ik}^{(b)} \quad \text{at the solid boundaries,} \tag{19}$$

can be redirected and satisfy the following three properties. (i) The vector magnitude is preserved, $|\boldsymbol{m}_{ik}^{(b)}| = |\boldsymbol{m}_{ik}|$. (ii) The orientation of the contact line is preserved, $\hat{\boldsymbol{\sigma}}_b \times \boldsymbol{m}_{ik}^{(b)} = \hat{\boldsymbol{\sigma}}_b \times \boldsymbol{m}_{ik}$, where $\hat{\boldsymbol{\sigma}}_b$ is the unitary outward surface area vector of the boundary. (iii) The angle between $\boldsymbol{m}_{ik}^{(b)}$ and $\hat{\boldsymbol{\sigma}}_b$, obeys the relation

$$\cos\theta_{ik} = \frac{\hat{\boldsymbol{\sigma}}_b \cdot \boldsymbol{m}_{ik}^{(b)}}{|\boldsymbol{m}_{ik}^{(b)}|}. \tag{20}$$

The thermodynamic and geometric approaches are consistent with the usual solid-fluid boundary conditions for the velocity and pressure fields, e.g., no-slip and impenetrability for the velocity field and $\hat{\boldsymbol{\sigma}}_b \cdot \boldsymbol{\nabla} p = 0$ for the pressure field.

4. Validation

The coupled system of advection and momentum equations of motion in Eqs. (2) and (3) are solved in an open-source, finite-volume solver with multiphase capabilities based on OpenFOAM-v2006 [53]. The simulations are performed using a second-order scheme for both temporal advancement and spatial discretisation.

The advection equations for the volume fraction fields were solved using the MULES algorithm for 3 sub-cycles with an interface compression coefficient of $c_\alpha = 1/2$ and a CFL condition of $Co = 0.1$.

A central differencing scheme is used to approximate the gradient, divergence and Laplacian operators, and a van Leer scheme [54] for the advection of the interface. All meshes are hexahedral with uniform grid spacing in every direction. The momentum equation is solved using the PISO-SIMPLE algorithm for coupling the pressure and velocity fields. The pressure is solved by an over-relaxation method with a relative tolerance of 10^{-7} for the pressure correction and 10^{-9} for the final pressure solution.

Unless specified, in all simulations, the kinematic viscosity is set to $\nu_A = \nu_C = 1 \times 10^{-6}\,\mathrm{m^2\,s^{-1}}$ and $\nu_B = 1.48 \times 10^{-5}\,\mathrm{m^2\,s^{-1}}$ and the density to $\rho_A = \rho_C = 1 \times 10^{3}\,\mathrm{kg\,m^{-3}}$ and $\rho_B = 1\,\mathrm{kg\,m^{-3}}$. Phases A and C correspond to liquids, whilst phase B represents a gas, such as air. The parameters for viscosity and density are chosen in analogy to water-air systems, which, universally, constitute the most familiar capillary system. However, this comes without loss of generality since the density and viscosity do not change the equilibrium states.

Validation Test 1: Force balance

The first validation test focuses on the balance of surface tension forces. A suspended binary droplet system surrounded by a gas is set up for this test. Therefore, no interfaces extend indefinitely, and the total surface tension forces should add up to zero over a volume containing the pair of droplets. This implies that the velocity of the centre of mass of the two droplets should persist during the relaxation to equilibrium, irrespective of their initial configuration. In this case, since no initial velocity is set on the system, the total momentum of the system should remain zero. The initial conditions of the system consist of two semicircles of equal area, each corresponding to phases A and C. The semicircles face each other and conform a complete circle embedded by phase B.

The two implementations are compared in order to demonstrate that the present surface tension force scheme is balanced correctly. Fig. 3 shows the comparison. The first implementation corresponds to an expression of the force that only includes the first term in Eq. (15). This implementation can be found in many multiphase VoF algorithms that follow the approach proposed in Refs [36–38]. The second implementation is the one proposed in this work, using the complete expression of Eq. (15). As can be observed from Fig. 3(a), the centre of mass accelerates for the curvature-only implementation, and the shape of the droplets does not conform to the expected equilibrium shape, where the interfaces have a constant curvature, for instance. The quantification of the displacement, $|\boldsymbol{X}_{\mathrm{cm}}(t) - \boldsymbol{X}_{\mathrm{cm}}(0)|$, is shown in Fig. 3(b), where the displacement of the droplet increases in time. Consequently, the acceleration of the centre of mass, $|\ddot{\boldsymbol{X}}_{\mathrm{cm}}|$, fluctuates about $10^2\,\mathrm{m\,s^{-2}}$. Moreover, a higher difference in surface tension produces a higher acceleration. Since there is no source of energy introduced to the system, this spontaneous propulsion is evidently unphysical.

In contrast, the same set of simulations using the proposed force model shows drastically different behaviour. Fig. 3(c) shows the binary droplet system at the expected equilibrium configuration, where the curvature is constant at every interface, which is the expected outcome that implies that the pressure has reached a constant value. Fig. 3(d) shows that the displacement of the centre of mass is negligible, which is expected since no momentum was initially given to the system, and, similarly, the acceleration is negligible.

Validation Test 2: Fluid-fluid contact angles

Then, the force scheme is tested to give the correct angles between interfaces provided a combination of surface tensions. For this validation test, a droplet immersed between two phases is set up so that the system relaxes to equilibrium, as shown in Fig. 4. The initial conditions of the system consist of a cube of side $L_x/4$ containing phase C, centred in the simulation domain and between phases A and B. The latter occupy the lower and upper half of the simulation domain. By changing the surface tensions γ_{AB} and γ_{BC} whilst keeping γ_{CA} constant, the angles between interfaces can be varied according to Neumann's construction. Taking the relation in Eq. (11) and employing the law of cosines, the relations

$$\cos\vartheta_A^{(e)} = \frac{\gamma_{BC}^2 - \gamma_{CA}^2 - \gamma_{AB}^2}{2\gamma_{CA}\gamma_{AB}}, \quad \cos\vartheta_B^{(e)} = \frac{\gamma_{CA}^2 - \gamma_{AB}^2 - \gamma_{BC}^2}{2\gamma_{AB}\gamma_{BC}}, \quad \cos\vartheta_C^{(e)} = \frac{\gamma_{AB}^2 - \gamma_{BC}^2 - \gamma_{CA}^2}{2\gamma_{BC}\gamma_{CA}}, \tag{21}$$

are obtained, where, as depicted in Fig. 4(b), the angles $\vartheta_i^{(e)}$ correspond to the expected contact angle at the triple point from the pair of interfaces ik and ij on the side of phase i. The measured contact angles are obtained from the intersection of the best-fitting circles.

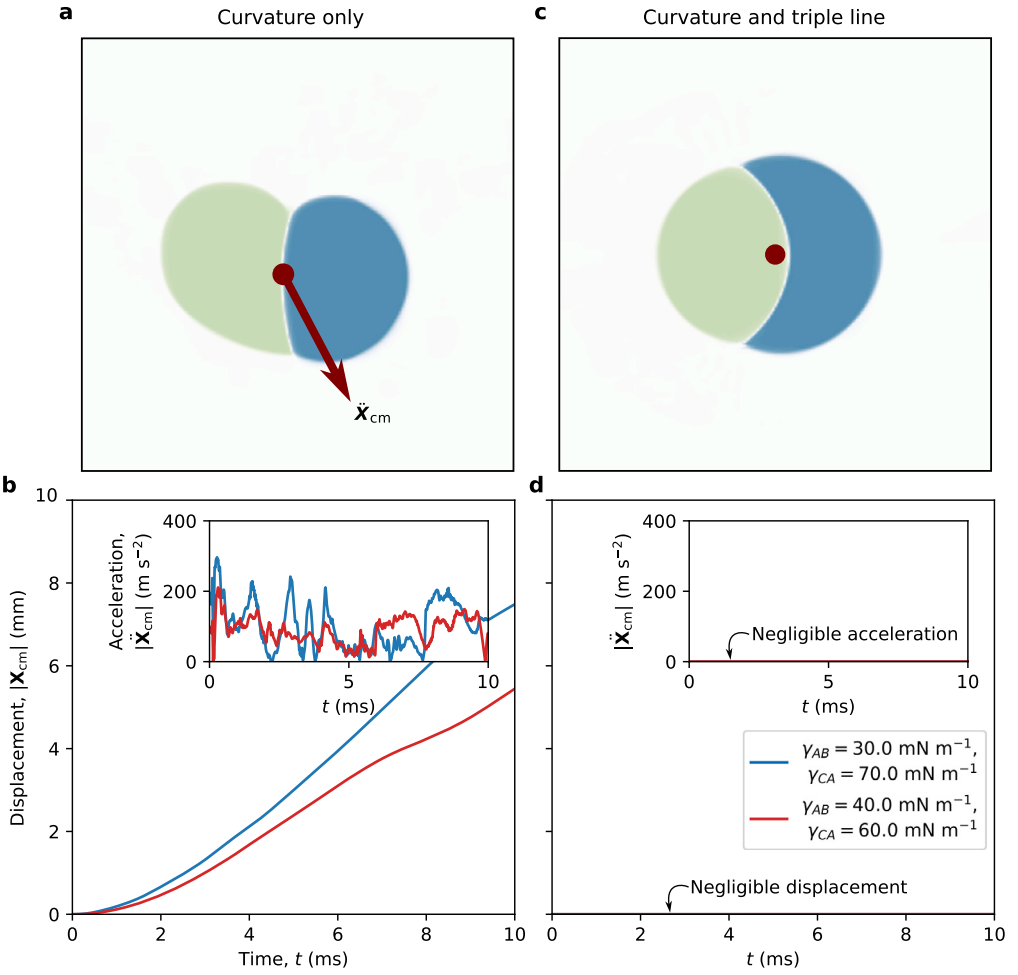

Fig. 3. Comparison between the curvature-only implementation and the force scheme proposed in the present work. Panels (a) and (c) correspond to snapshots after $t = 10$ ms, of a binary droplet with different models for the surface tension forces: (a) curvature-only expression, i.e., the first term in Eq. (15) and (c) corresponds to the full expression. The red arrows show the acceleration of the centre of mass of the binary droplet system. Panels (b) and (d) displacement of the centre of mass from its initial position and the magnitude of its acceleration (inset) as a function of time for two different pairs of surface tensions. The simulation domain is 2D, with size $L_x \times L_y = 1\,\text{mm}^2$ in a $N_x \times N_y = 200^2$ mesh. Periodic boundary conditions are set in all directions. The surface tension for the BC interface is $\gamma_{BC} = 50\,\text{mN m}^{-1}$. (Colour online)

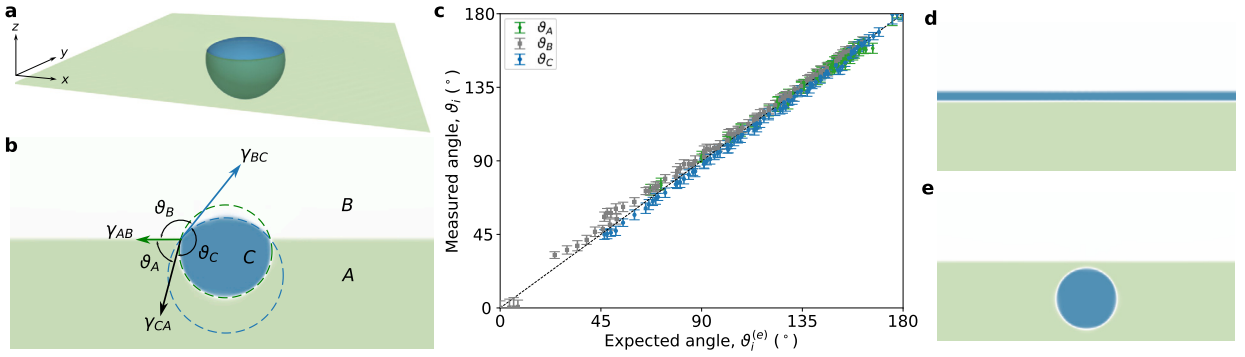

Fig. 4. Measurement of the Neumann angles for the angles between the interfaces in a liquid lentil numerical experiment. (a) Three-dimensional simulation of a liquid lentil. (b) Slice of the system in (a) at the plane passing through the centre of phase C and perpendicular to the AB interface. Depending on the surface tensions, the interfaces relax to the angles ϑ_A, ϑ_B and ϑ_C at the triple line. (c) Plot of the distribution of the measured angles against the expected angles according to Neumann's construction. (d) Complete spreading of phase C between phases A and B. (e) Complete detachment of phase C from the AB interface. The system dimensions and mesh resolution are $L_x \times L_y \times L_z = 2 \times 2 \times 1\,\text{mm}^3$ and $N_x \times N_y \times N_z = 128 \times 128 \times 64$, respectively. Periodic boundary conditions are assigned along x and y, and solid walls at the top and bottom boundaries. The surface tensions for γ_{AB} and γ_{BC} vary from 20 to 120 mN m^{-1}, and $\gamma_{CA} = 40\,\text{mN m}^{-1}$. (Colour online)

The technique employed to extract the contact angles, ϑ_i, is by calculating the intersection angles of the two fitted circles as shown in Fig. 4(b), e.g., to the pair of interfaces CA and BC for ϑ_C. Each circle is obtained by a least squares algorithm from the isosurface $\alpha_i = 1/2$ in the following way. Each volume fraction isosurface is obtained by a marching squares algorithm along a slice that passes through the centre of the liquid lentil. This results in a set of points, $P_j = \{\boldsymbol{x}_n\}, n \in \mathbb{N}$, $j = \{BC, CA\}$. Then, the distance, R_n, from each of the points in the set to a new point, $\boldsymbol{x}_c$, is calculated

$$R_n(\boldsymbol{x}_c) := |\boldsymbol{x}_n - \boldsymbol{x}_c| \qquad \forall\, \boldsymbol{x}_n \in P_j. \tag{22}$$

For which, the residue function

$$f(\boldsymbol{x}_c) := \sum_n \left[R_n(\boldsymbol{x}_c) - \langle R_n \rangle\right]^2, \tag{23}$$

where $\langle \cdot \rangle$ denotes the average value, is minimised, which is by finding the roots of $\partial f / \partial \boldsymbol{x}_c$. Consequently, the point $\boldsymbol{x}_c$ corresponds to the centre of the best-fitting circle and its radius is obtained by reevaluating $\langle R_n \rangle$. The uncertainty associated with the fit corresponds to the residue defined in Eq. (23). Lastly, the fluid-fluid contact angles are calculated from the unitary tangent vectors at the intersection points between the circles. This also implies that the contact angles inherit uncertainty from the covariance of the values of the centre and radius of each fitted circle. Fig. 4(c) compares the three contact angles and the uncertainty from their calculation. It can readily be observed that there is good agreement with the expected angles.

Without loss of generality, note that if $\gamma_{AB} > (\gamma_{BC} + \gamma_{CA})$, Eq. (21) is no longer valid as it would imply that $\cos\vartheta_C > 1$. Instead, a transition to complete spreading occurs, and the triple line vanishes. This implies that $\vartheta_C = 0$, and phase C forms a film separating the A and B phases. Similarly, if $\gamma_{CA} > (\gamma_{AB} + \gamma_{BC})$, phase C forms a suspended spherical droplet next to the AB interface. The proposed model for the surface tension forces captures such phenomena well, as shown in Figs. 4(d) and (e), respectively.

In Appendix D, the grid convergence of the forces scheme for the fluid-fluid contact angle is assessed. It can be readily observed in Fig. D.10 that the action of the surface tension forces is robust upon the coarsening of the grid. The angles calculated achieve a nearly converged state on the second coarsest grid while the measurement uncertainty consistently reduces with decreasing grid size.

Validation Test 3: Fluid-solid contact angles

After validating the algorithm for the angles between interfaces, partially wetting boundary conditions are now tested. The results are shown in Fig. 5. For this, the contact angle against a flat solid surface is compared against the expected value given by the boundary condition. Two implementations for prescribing the wettability of the surface are considered as discussed in the previous section: the thermodynamic and the geometric approaches. The initial conditions of the system consist of a cube of side $L_x/4$ of phase A sessile to the solid surface, but otherwise, centred at the simulation domain.

For the first case, the contact angle against a given combination of surface tensions is measured. Let us assume that, as in Eq. (21), a relation between the three surface tensions and the contact angle is a function of the surface tensions, i.e., $\cos\theta_{ik} = f(\gamma_{kS}, \gamma_{iS}, \gamma_{ik})$ for some function f. In particular,

$$\cos\theta_{ik} = \beta_1 \left(\frac{\gamma_{kS} - \gamma_{iS}}{\gamma_{ik}}\right) + \beta_3 \left(\frac{\gamma_{kS} - \gamma_{iS}}{\gamma_{ik}}\right)^3, \tag{24}$$

is proposed for the partial-wetting regime, i.e., when the right-hand side is between -1 and 1. Here, where β_1 and β_2 are introduced as fitting parameters. Setting γ_{AB} and γ_{AS} and varying γ_{BS} for two sets of simulations gave the results in Fig. 5(b). By fitting, $\beta_1 = 1.37$ and $\beta_3 = 2.15$, a good representation for the curve and the complete spreading regime was found. Additionally, complete spreading and dewetting were found for $(\gamma_{kS} - \gamma_{iS}) \geq 0.52\gamma_{ik}$ and $(\gamma_{kS} - \gamma_{iS}) \leq -0.51\gamma_{ik}$.

Next, the geometric approach for prescribing the contact angle is assessed. As shown in Fig. 5(c), resetting the angle of $\boldsymbol{m}_{AB}$ with respect to the unitary normal of the surface prescribes the contact angle. This approach is independent of the expression of the surface tension forces. Therefore, the present model for the surface tension forces in Eq. (15) is demonstrated do be compatible with the geometric approach. Fig. 5(d) shows the measured contact angle, θ_{AB}, against the prescribed contact angle, $\theta_{AB}^{(p)}$, and good agreement can be observed.

The geometric approach gives accurate results for a partially wetting boundary condition, i.e., prescribing a finite contact angle. Nonetheless, the thermodynamic approach, whilst covering the partial wetting regime, can be extended to complete wetting or dewetting. Additionally, specifying the surface tensions of the solid against the different fluid phases relaxes the contact angles and prevents the self-propulsion of multiple sessile droplets [55]. In other words, the Girifalco-Good relations [56] are naturally satisfied by the thermodynamic approach.

As shown in Fig. 5c, for both algorithms prescribing the boundary conditions, the contact angle was measured by the best circle fit obtained as explain in by Eq. (23). Appendix E shows the equilibrium contact angles for different grid sizes. Whilst the expected steady-state is nearly obtained from the second coarsest grid, the uncertainty in the calculation of the angles decreases with the grid size.

Validation Test 4: Error estimation of the surface tension forces

In this subsection, the numerical error from two different implementations of VoF is assessed in a similar fashion to Evrard et al. [57] and Cifani et al. [58]. In order to do this, a case with a known analytic solution is constructed, for instance, a two-dimensional

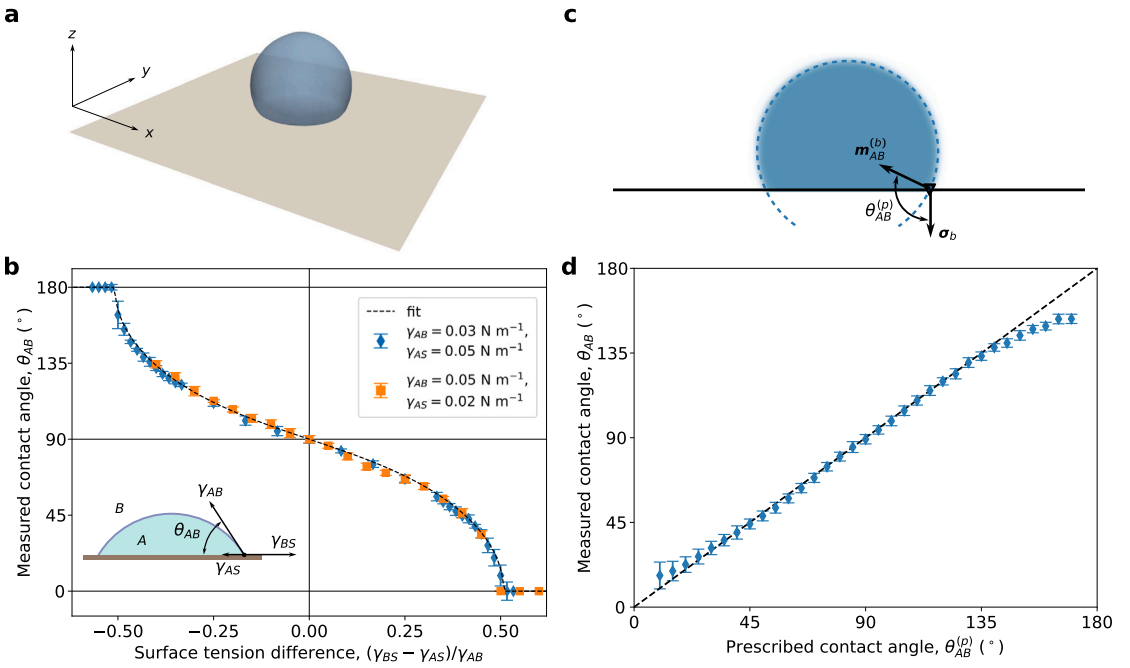

Fig. 5. Contact angles of a gas-liquid system in contact with a solid. (a) and (b) Three-dimensional simulation of a droplet on a solid surface. The solid surface can be modelled as an additional phase prescribing the boundary condition. Thus, the contact angle can be specified by specifying the solid-gas and solid-liquid surface tensions. (b) Plot of the measured contact angle as a function of the surface tension difference by varying the surface tension between the gas and the solid, γ_{BS}. The dashed line corresponds to the best fit using Eq. (24). (c) and (d) In contrast to the simulations in panel (a) and (b), the angle, $\theta_{AB}^{(p)}$, of the normal vector of the liquid-gas interface and the solid surface is directly specified as a boundary condition, here shown for a slice at the centre of the droplet. (d) Plot of the measured and the prescribed contact angles. For reference, the identity function corresponds to the dashed line. The simulation dimensions and mesh resolution in all panels are $L_x \times L_y \times L_z = 2 \times 2 \times 0.75\,\text{mm}^3$ and $N_x \times N_y \times N_z = 128 \times 128 \times 48$. Periodic boundary conditions are defined along x and y, a solid for the bottom boundary and open at the top. The system relaxes for 150 ms. (Colour online)

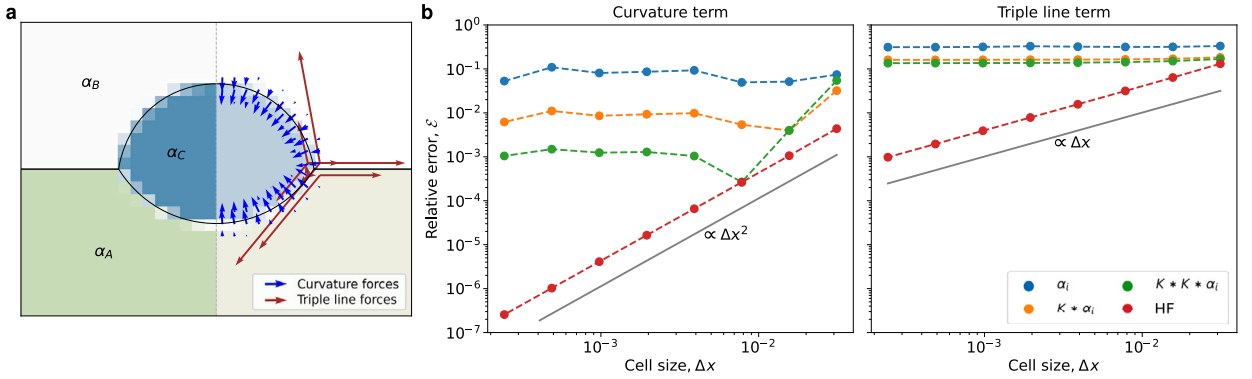

Fig. 6. Error for different VoF implementations in the calculation of the forces. (a) Profiles of the analytical computation of the volume fraction fields, α_i for $i = A, B, C$, and the distribution of forces on a 64×48 grid. The black curves represent the interfaces, and the colour map indicates the partial filling of the corresponding cell by the phase as in Fig. 4. The blue and brown arrows represent the curvature and triple line forces as expressed by the first and last term of Eq. (15), respectively. (b) Relative error in the calculation of the forces as a function of the cell size, Δx. Four cases are shown; the first three correspond to a straight calculation of the forces using a finite differences stencil for no filtering, once and twice iterative application of a smoothing filter as denoted by α_i, $K * \alpha_i$ and $K * K * \alpha_i$, respectively. The last case corresponds to a preliminary Height-Function algorithm to calculate the curvature and triple line terms described in Appendix C. (Colour online)

liquid lentil, as in Validation Test 2 of the present section. As shown in Fig. 6(a), by knowing the equilibrium configuration for the shape of each interface in the system, the corresponding volume fraction fields α_i, $i = A, B, C$, are obtained by analytical integration.

The contribution to the surface tension forces from the curvature can be expressed as

$$\boldsymbol{f}_{\text{curv}} = \sum_{i=1}^{M} \sum_{k=i+1}^{M} \gamma_{ik}\, \kappa_{ik}\, \boldsymbol{n}_{ik}\, \delta_{ik}^{(S)}, \tag{25}$$

and the force at the triple line as

$$\boldsymbol{f}_{\mathrm{tl}} = \sum_{i=1}^{M} \sum_{k=i+1}^{M} \gamma_{ik}\, \hat{\boldsymbol{t}}_{ik}\, \delta_{ik}^{(L)}, \tag{26}$$

where the different elements in Eqs. (25) and (26) can be evaluated by different methods as it will be described in the following.

As discussed in Section 2, the sharpness of the interface in the algebraic VoF is recovered by means of the interface compression coefficient, c_α. At low values of c_α, the interface diffuses; this effect is emulated systematically through a smoothing filter,

$$\tilde{\alpha}_i(\boldsymbol{x}_{m,n}) = (K * \alpha_i)(\boldsymbol{x}_{m,n}) = \sum_{m'} \sum_{n'} K(m-m', n-n')\, \alpha_i(\boldsymbol{x}_{m',n'}) \tag{27}$$

where $\boldsymbol{x}_{m,n}$ is the centre position vector of the cell (m,n). The smoothing filter employed is

$$K(m,n) = \begin{cases} w & \text{if } |m| \leq 1 \text{ and } |n| \leq 1 \\ 0 & \text{otherwise} \end{cases}, \tag{28}$$

for some constant, w, such that $\sum_{m,n} K(m,n) = 1$. In this two-dimensional uniform grid, $w = 1/9$, which corresponds to the average in a 3×3 neighbourhood of the volume fraction. Note that the filter can be applied iteratively to the volume fraction fields to smooth out the interfaces further. After the smoothing filter is applied to α_i, the forces can be calculated using Eq. (15).

Another common approach to calculate the surface tension forces is by a Height Function algorithm [59–61]. A preliminary adaptation of the Height Function method, aimed at proving compatibility with the force scheme, is presented in this work. Moreover, as it will be shown, it promises that high-order accuracy in the calculation of the forces can be achieved by grid refinement. In summary, a Height Function, H, is evaluated in the neighbourhood of the ik-interface. This leads to a subgrid distance to the interface from a reference point, and therefore, the curvature, normal vector and tangent vectors can be evaluated with increasing accuracy. The details of the method can be found in Appendix C. Nonetheless, $\delta_{ik}^{(S)}$ and $\delta_{ik}^{(L)}$ are still calculated by means of Eqs. (12) and (16), respectively.

Once the surface tension forces are calculated, an estimation of the error corresponding to each term, i.e., curvature and triple line contributions, can be estimated. The relative error in the curvature component can be defined as

$$\mathcal{E}_{\mathrm{curv}} := \frac{\int_\Omega \left| \boldsymbol{f}_{\mathrm{curv}} - \boldsymbol{f}_{\mathrm{curv}}^{(e)} \right| \mathrm{d}V}{\int_\Omega |\boldsymbol{f}_{\mathrm{curv}}^{(e)}|\, \mathrm{d}V}. \tag{29}$$

Similarly, the relative error for the forces at the triple line can be defined as

$$\mathcal{E}_{\mathrm{tl}} := \frac{\int_\Omega \left| \boldsymbol{f}_{\mathrm{tl}} - \boldsymbol{f}_{\mathrm{tl}}^{(e)} \right| \mathrm{d}V}{\int_\Omega |\boldsymbol{f}_{\mathrm{tl}}^{(e)}|\, \mathrm{d}V}, \tag{30}$$

where the superscript, (e), in the forces corresponds to the expected value from the analytical solution. For an equilibrium configuration, such as the case under analysis, the total components of the surface tension forces are expected to vanish independently. Therefore, any residual force is numerical in origin, i.e., $\int \boldsymbol{f}_{\mathrm{curv}}^{(e)}\, \mathrm{d}V = \int \boldsymbol{f}_{\mathrm{tl}}^{(e)}\, \mathrm{d}V = 0$.

Fig. 6(b) shows the relative errors for the curvature and triple line contributions. It can be observed that the computation of the forces directly from the divergence of the unit normal vector leads to a poor representation of the surface tension forces. Refining the grid by decreasing the cell size, Δx, does not reduce the error. For the curvature calculation, this phenomenon has been reported before [58], and it is only by smoothing out the volume fraction fields that the error is reduced. However, for the triple line forces, an additional effect takes place. In the neighbourhood of any triple line, since three phases intersect in a wedge, refining the grid results in a self-similar picture, which is invariant with respect to the grid size. Therefore, as Δx goes to zero, a reduction in the error is not expected.

A reduction of the error in the forces by a smoothing filter is expected in general since a requirement for convergence in finite differences or finite volume schemes is the continuity of the field in which the derivatives are approximated. As the interfaces are diffused, the discontinuity in the volume fractions is reduced, and the discretisation schemes work better. In conclusion, the convergence of the curvature and triple line forces evaluated by finite differences on the volume fractions is of zeroth order with respect to grid size. However, smoothing out the volume fraction fields reduces the numerical error significantly. This can be done by applying a smoothing filter or by using a low value of the interface compression coefficient, c_α, as it will be shown in Appendix D.

When using the Height Function method, the curvature term has a second-order convergence on the grid size, as expected for a three-point stencil [57,59]. However, the challenge of finding the position of the triple line at the subgrid level emerges. For example, circumventing this issue by linear extrapolation results in a first-order convergence in the representation of the forces. Therefore, higher-order schemes or a better subgrid localisation of the triple line will improve the convergence of the force scheme.

In contrast to several existing studies that deal with an arbitrary number of phases [21–23], convergence analyses of the force scheme at the triple line are carried out in this work. These analyses were performed on an idealised system and the numerical solutions shown in Appendices D–F. The results show the promising adaptability and reliability of the proposed surface tension forces for different flavours of VoF, such as algebraic or geometric/Height Function algorithms.

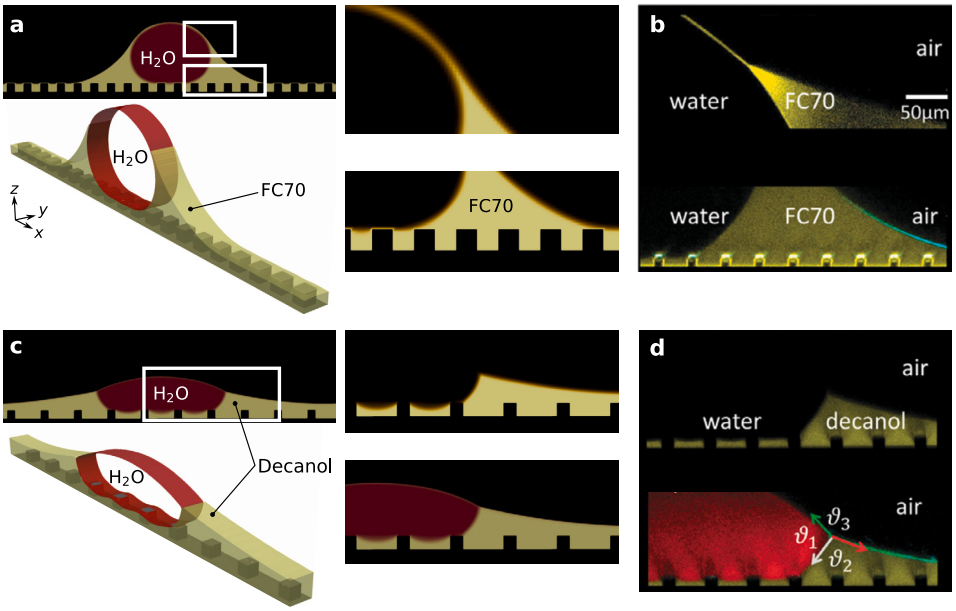

Fig. 7. Simulations of Lubricant-Impregnated Surfaces (LIS). (a) and (b) are pseudo-2D simulations of a water droplet on top of a periodic array of pillars coated by FC70 lubricant in equilibrium. (a) Corresponds to the numerical simulations using the proposed force scheme by showing the volume fraction of the two liquids along the central slice of the simulation domain. The water and lubricant are plotted in red and yellow, respectively. Additionally, the interfaces are shown as the isosurfaces at $\alpha_i = 0.5$. In the close-up, the volume fraction of the FC70 is highlighted exclusively to show the presence of the lubricant surrounding the droplet and the solid surface. (b) Confocal images by Schellenberger et al. from Fig. 4 of Ref. [13] showing the cloaking of the droplet by the FC70 indicated by the fluorescent signal. (c) and (d) are similar to (a) and (b), the surface is coated by decanol. The numerical simulations are shown in (c), and the confocal images of the experiments in (d) were also taken from Fig. 4 of Ref. [13]. The system parameters are summarised in Table 1. (Colour online)

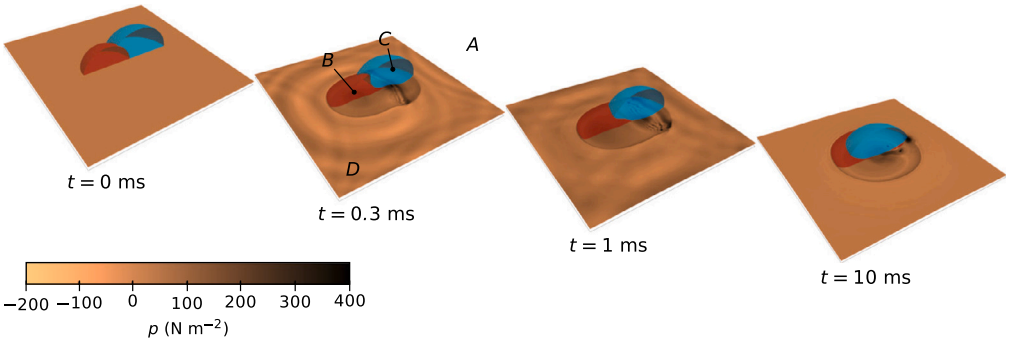

Fig. 8. Evolution of a four-phase LIS. A droplet of liquid *B* (red isosurface) is in contact with another droplet of liquid *C* (blue isosurface) and a third liquid, *D*, all surrounded by a gas *A*. Liquid *D* works as a lubricant by coating the solid surface underneath, and it is coloured by the local pressure field at the interface. The simulation parameters are summarised in Table 2. (Colour online)

Simulations of liquid-infused surfaces

Finally, simulations of lubricant-impregnated surfaces (LIS) are performed using the newly proposed method and shown in Fig. 7. For simplicity, the term LIS will be referred as a more general term that includes Slippery Liquid-Infused Porous Surface (SLIPS) and other types of surfaces in which an immiscible liquid of finite thickness alleviates the friction of sessile droplets against the solid. These systems are addressed in this work to show the correct modelling of the spreading of the lubricant on the solid with the droplet, preventing the formation of a contact line. A feature that is essential to these types of surfaces [14].

The simulation results are compared against the equilibrium configuration of a sessile droplet on a lubricated surface against the experimental observations by Schellenberger et al. [13]. On the one hand, it can be observed in Figs. 7(a) and 7(b) that the lubricant spreads on the droplet by cloaking it. In the simulations, the volume fraction of the lubricant that covers the top of the droplet is finite. However, as shown by isosurface $\alpha_{\text{FC70}} = 1/2$, the value of the volume fraction does not reach unity as a fully developed phase which gives the appearance of a finite contact angle. A similar effect is observed in the confocal images, in which a film of an estimated thickness of 20 nm is found in the aforementioned experiments. On the other hand, Figs. 7(c) and 7(d) show different behaviours in the case of a decanol LIS. Here, a Neumann triangle of finite contact angles is formed; thus, the lubricant does not

Table 1
Simulation parameters for Fig. 7(a) and 7(c), taken from Ref. [13].

System dimensions and mesh resolution		
$L_x \times L_y \times L_z$	=	$4 \times 0.2 \times 2\,\mathrm{mm}^3$
$N_x \times N_y \times N_z$	=	$320 \times 16 \times 160$
Relax. time	=	100 ms
Int. comp. c_a	=	1.0
Periodic boundary conditions along x and y, solid walls at $z = 0$ and pillars and open at the top boundary.		
Physical parameters		
ν_{water}	=	$1 \times 10^6\,\mathrm{m^2\,s^{-1}}$
ν_{air}	=	$1.48 \times 10^5\,\mathrm{m^2\,s^{-1}}$
ν_{FC70}	=	$11.0 \times 10^6\,\mathrm{m^2\,s^{-1}}$
ν_{decanol}	=	$14.5 \times 10^6\,\mathrm{m^2\,s^{-1}}$
ρ_{water}	=	$1 \times 10^3\,\mathrm{kg\,m^{-3}}$
ρ_{air}	=	$1\,\mathrm{kg\,m^{-3}}$
ρ_{FC70}	=	$1.93 \times 10^3\,\mathrm{kg\,m^{-3}}$
ρ_{decanol}	=	$830\,\mathrm{kg\,m^{-3}}$
$\gamma_{\text{water air}}$ (FC70)	=	$72\,\mathrm{mN\,m^{-1}}$
$\gamma_{\text{water air}}$ (decanol)	=	$30.1\,\mathrm{mN\,m^{-1}}$
$\gamma_{\text{FC70 air}}$	=	$17.9\,\mathrm{mN\,m^{-1}}$
$\gamma_{\text{decanol air}}$	=	$28.5\,\mathrm{mN\,m^{-1}}$
$\gamma_{\text{water FC70}}$	=	$52.8\,\mathrm{mN\,m^{-1}}$
$\gamma_{\text{water decanol}}$	=	$8.6\,\mathrm{mN\,m^{-1}}$
$\theta_{\text{water decanol}}$	=	158°
$\theta_{\text{water air}}$	=	160°

Table 2
Simulation parameters for Fig. 8. Arbitrary values for demonstration.

System dimensions and mesh resolution		
$L_x \times L_y \times L_z$	=	$2 \times 2 \times 1\,\mathrm{mm}^3$
$N_x \times N_y \times N_z$	=	$96 \times 96 \times 48$
Relax time	=	10 ms
Periodic boundary conditions along x and y, solid walls at $z = 0$ and pillars and open at the top boundary.		
Physical parameters		
ρ_{D}	=	$1 \times 10^3\,\mathrm{kg\,m^{-3}}$
ν_{D}	=	$1.0 \times 10^6\,\mathrm{m^2\,s^{-1}}$
γ_{AB}	=	$72\,\mathrm{mN\,m^{-1}}$
γ_{AC}	=	$66\,\mathrm{mN\,m^{-1}}$
γ_{AD}	=	$18\,\mathrm{mN\,m^{-1}}$
γ_{BC}	=	$56\,\mathrm{mN\,m^{-1}}$
γ_{BD}	=	$44\,\mathrm{mN\,m^{-1}}$
γ_{CD}	=	$31\,\mathrm{mN\,m^{-1}}$

spread over the droplet or the micropillar array. In conclusion, the numerical simulations are in good qualitative agreement with the experimental observations by Schellenberger et al. [13].

To illustrate the method's capabilities further, a four-phase LIS system is shown in Fig. 8. In this case, liquid that completely wets a solid surface is considered (D) and a pair of immiscible droplets placed on the lubricant and relaxing to equilibrium. The gas phase, A, surrounds the rest of the liquids B, C and D, where the droplets correspond to B and C. It can be observed how the droplets interact with each other and how the lubricant reconfigures itself, raising a meniscus around the droplets and allowing the droplets to find equilibrium.

To test the convergence of the force scheme, a comparison for different grid sizes is show them in Appendix F for the two cases presented in Figs. 7(a) and 7(c). As expected, the quantitative discrepancies are negligible with respect to the grid size, and the system settles at the expected equilibrium configuration.

5. Conclusions

In this work, a new model for incorporating surface tension forces for an arbitrary number of phases in the Volume-of-Fluid (VoF) methodology has been developed and tested. Based on the macroscopic action of surface tension, this approach is demonstrated to be consistent with the laws of motion. The proposed model accurately produces the forces at the triple line but the reduction to a two- or single-phase flow has been shown.

The efficacy of the proposed algorithm is bestowed by using three quantitative and one qualitative validation tests. Consistency with Newton's laws of motion is shown by means of a suspended capillary system relaxing to equilibrium. As shown in the numerical experiment, the total momentum of the system is a conserved quantity, which can only occur due to the correct balance of forces. Subsequently, it was shown that the forces at the triple line, which adjust the contact angles according to Neumann's construction, are correctly captured. In consequence, this technique was further employed to prescribe the contact angle against a solid phase by adjusting their respective surface tension constants. Additionally, it is shown that this allows to emulate the complete spreading or dewetting of the fluids-on-fluids or fluids-on-solids. This phenomenon is consistent with the thermodynamic behaviour of a multiphase system and emerges naturally from the proposed formulation. Alternatively, the contact angle can be prescribed by readjusting the direction of the gradient vector of the volume fraction field with accurate results.

A brief analysis of the error in representing the forces was carried out. The convergence of the force scheme for different grid resolutions has been demonstrated and assessed in terms of the contact angle for three different systems. This analysis was done on the curvature and triple line terms separately. A significant reduction in the error can be observed by smoothing the volume fractions. Additionally, the compatibility of the force scheme with other methods was demonstrated by adapting a simple Height Function algorithm to the triple line term. This approach shows promising results for convergence to the expected force fields. The importance of the line and surface density functions should be emphasised; these distribute the one- and two-dimensional force fields corresponding to the triple line and curvature components into the three-dimensional space.

Finally, the new formulation was applied to simulate a multiphase system, a lubricant-impregnated surface. Agreement between the simulation results and previous experimental observations by Schellenberger et al. [13] was demonstrated. For complete spreading, as in the case of an FC70 LIS, the droplet is cloaked by the lubricant. Also, a Neumann triangle is formed at the triple line for partial spreading, as in the case of a decanol-lubricated surface. Afterwards, for illustration purposes, the algorithm was applied to a four-phase LIS system in which two immiscible droplets interact, referring to the extensibility of the method to more than three phases.

CRediT authorship contribution statement

Élfego Ruiz-Gutiérrez: Writing – review & editing, Writing – original draft, Visualization, Validation, Software, Methodology, Investigation, Formal analysis, Conceptualization. **Josef Hasslberger:** Writing – review & editing, Software, Methodology, Investigation, Formal analysis. **Markus Klein:** Writing – review & editing, Validation, Methodology, Investigation, Conceptualization. **Kenny Dalgarno:** Writing – review & editing, Project administration, Funding acquisition. **Nilanjan Chakraborty:** Writing – review & editing, Supervision, Resources, Project administration, Methodology, Funding acquisition, Formal analysis.

Declaration of competing interest

The authors declare that they have no known competing financial interests or personal relationships that could have appeared to influence the work reported in this paper.

Data availability

The data supporting the findings in this study are available from the authors upon reasonable request.

Acknowledgements

The authors are grateful for the financial support from EPSRC (EP/V013092/1) and for computational support to ARCHER2 (EP/R029369/1) and Rocket HPC.

Appendix A. Derivation of the surface tension forces expression

In van der Waals's theory of capillarity, the Helmholtz free energy density of a system can be expressed as

$$\psi(\boldsymbol{x}) \sim W(\alpha, T) + \frac{1}{2} K(T) |\boldsymbol{\nabla}\alpha|^2, \tag{A.1}$$

where T is the system's temperature, and K is a coefficient related to the direct correlation between the molecules of the fluid mixture. Here, $\alpha = \alpha(\boldsymbol{x})$ is utilised as the phase field; therefore, it is a smooth function of space. $W(\alpha, T)$ corresponds to the excess free energy density and has the shape of a double-well function for α, that is, $W(\alpha, T) = 0$ if $\alpha = 0$ or 1 and $W(\alpha, T) > 0$ otherwise [62]. The profile of α in the thermodynamic equilibrium can be obtained by the Euler-Lagrange equations, assuming that the chemical potential, $\mu := \partial_\alpha W - K\nabla^2\alpha$, is constant everywhere. Fig. A.9(a) shows a schematic solution for α.

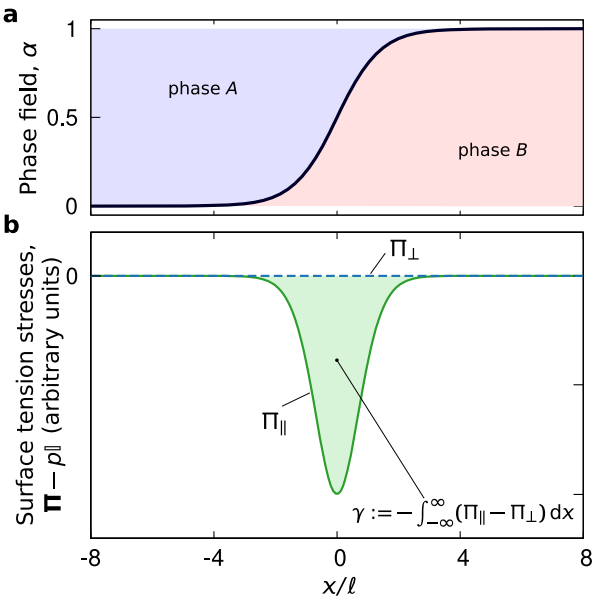

Fig. A.9. Illustration of the stresses and the mechanical definition of the surface tension for a flat interface. a) Schematic representation of the transition between phases A to B as given by the phase field variable α. In this case, $\alpha = 0$ represents phase A, whereas $\alpha = 1$ corresponds to phase B. The transition occurs over a characteristic length scale ℓ, known as the interface thickness. b) Profile of the surface tension stresses along the normal coordinate to the interface. The area under the curve, highlighted as the green-shaded region, defines the surface tension. (Colour online)

The tensor $\boldsymbol{\Pi}$, sometimes called the pressure tensor, becomes a conserved quantity of the Euler-Lagrange equations and has the form [63],

$$\boldsymbol{\Pi} = (\alpha\,\mu - W)\,\mathbf{I} + K\left(\boldsymbol{\nabla}\alpha \otimes \boldsymbol{\nabla}\alpha - \frac{1}{2}|\boldsymbol{\nabla}\alpha|^2\mathbf{I}\right), \tag{A.2}$$

$$= p\,\mathbf{I} + K\left[\boldsymbol{\nabla}\alpha \otimes \boldsymbol{\nabla}\alpha - \left(\frac{1}{2}|\boldsymbol{\nabla}\alpha|^2 + \alpha\nabla^2\alpha\right)\mathbf{I}\right], \tag{A.3}$$

such that, in mechanical equilibrium, $\boldsymbol{f}_{\mathrm{st}} = -\boldsymbol{\nabla}\cdot\boldsymbol{\Pi} = 0$ everywhere. Here, the bulk pressure, $p := \alpha(\partial_\alpha W) - W$ is defined from the equation of state of a homogeneous system. Fig. A.9(b) depicts a schematic representation of the stresses due to surface tension. Then, according to Tolman [64], the surface tension between the two phases can be defined by the integral expression,

$$\gamma := -\int_{-\infty}^{\infty} \left(\Pi_{\parallel} - \Pi_{\perp}\right)\,\mathrm{d}x, \tag{A.4}$$

where $\Pi_{\parallel} := \hat{\boldsymbol{t}}\cdot\boldsymbol{\Pi}\cdot\hat{\boldsymbol{t}}$ is a parallel component to the interface, and $\Pi_{\perp} := \hat{\boldsymbol{n}}\cdot\boldsymbol{\Pi}\cdot\hat{\boldsymbol{n}}$ is the normal component. The definition of surface tension from Eq. (A.4) has the advantage that it is not restricted to a flat interface.

However, if the surface tension is known, the task is reduced to reconstructing $\boldsymbol{\Pi}$. This approach is considered by Lafaurie et al. [31], Scardovelli and Zaleski [30] and Tryggvason et al. [28]. For example, the stresses on an infinitesimally narrow, flat interface, which is perpendicular to the x coordinate, can be written as $\Pi_{\parallel} = p - \gamma\delta(x)$ and $\Pi_{\perp} = p$. Combining the two components into a single expression, the stresses can be generalised as

$$\boldsymbol{\Pi} = -\gamma\,(\mathbf{I} - \hat{\boldsymbol{n}}\otimes\hat{\boldsymbol{n}})\,\delta(S(\boldsymbol{x})), \tag{A.5}$$

where the interface is defined over a surface, S, with normal vector $\hat{\boldsymbol{n}}$. Note that p can be replaced by the hydrodynamic pressure of an incompressible flow already included in the Navier-Stokes equations (3).

Since each interface has a different surface tension coefficient, $\boldsymbol{\Pi}$ can be made specific to each interface. Therefore, adding the subindices ik to all the quantities, e.g., $\boldsymbol{\Pi} \to \boldsymbol{\Pi}_{ik}$ for the ik-interface is proposed for this effect. In this way, the surface tension forces are derived from the superposition of the stresses of all interface pairs, and the expression in Eq. (5) is recovered.

Arriving at Eq. (15) from Eq. (5) is done directly by substituting the definitions of $\boldsymbol{m}_{ik}$ and $\delta_{ik}^{(S)}$,

$$\boldsymbol{f}_{\mathrm{st}} = \boldsymbol{\nabla}\cdot\sum_{i=1}^{M}\sum_{k=i+1}^{M}\gamma_{ik}(\mathbf{I} - \hat{\boldsymbol{n}}_{ik}\otimes\hat{\boldsymbol{n}}_{ik})|\boldsymbol{m}_{ik}| = \sum_{i=1}^{M}\sum_{k=i+1}^{M}\gamma_{ik}\boldsymbol{\nabla}\cdot(|\boldsymbol{m}_{ik}|\mathbf{I} - \hat{\boldsymbol{n}}_{ik}\otimes\boldsymbol{m}_{ik}) + |\boldsymbol{m}_{ik}|(\mathbf{I} - \hat{\boldsymbol{n}}_{ik}\otimes\hat{\boldsymbol{n}}_{ik})\boldsymbol{\nabla}\gamma_{ik}, \tag{A.6}$$

where the first term inside the sum can be expanded using vector calculus identities into

$$\nabla \cdot (|\boldsymbol{m}_{ik}|\mathbf{I} - \hat{\boldsymbol{n}}_{ik} \otimes \boldsymbol{m}_{ik}) = \left[\frac{\nabla(\boldsymbol{m}_{ik} \cdot \boldsymbol{m}_{ik})}{2|\boldsymbol{m}_{ik}|} - \boldsymbol{m}_{ik}(\nabla \cdot \hat{\boldsymbol{n}}_{ik}) - (\hat{\boldsymbol{n}}_{ik} \cdot \nabla)\boldsymbol{m}_{ik} \right] \tag{A.7}$$

$$= \hat{\boldsymbol{n}}_{ik} \times (\nabla \times \boldsymbol{m}_{ik}) - \boldsymbol{m}_{ik}(\nabla \cdot \hat{\boldsymbol{n}}_{ik}). \tag{A.8}$$

Then, by the definition of $\boldsymbol{m}_{ik} := \alpha_k \nabla \alpha_i - \alpha_i \nabla \alpha_k$, the curl term becomes,

$$\nabla \times \boldsymbol{m}_{ik} = \nabla \times (\alpha_k \nabla \alpha_i - \alpha_i \nabla \alpha_k) \tag{A.9}$$

$$= \alpha_k \nabla \times \nabla \alpha_i + (\nabla \alpha_k) \times \nabla \alpha_i - \alpha_i \nabla \times \nabla \alpha_k - (\nabla \alpha_i) \times \nabla \alpha_k \tag{A.10}$$

$$= 2 \nabla \alpha_k \times \nabla \alpha_i \tag{A.11}$$

Finally, by substituting the previous expressions, the expression in Eq. (15) is obtained.

Appendix B. The surface and line density functions

The following exposition is based on Brackbill et al. [45] in which the surface and line density functions are constructed by means of a smoothing kernel of continuous input, K.

Let $K : \mathbb{R}^3 \to \mathbb{R}^+$ be a smooth isotropic convolution kernel such that

$$\tilde{f}(\boldsymbol{x}) = (K * f)(\boldsymbol{x}) := \int_{\mathbb{R}^3} f(\boldsymbol{x}') K(\boldsymbol{x} - \boldsymbol{x}') \, \mathrm{d}V' \tag{B.1}$$

produces a field, $\tilde{f}$, to vary smoothly everywhere in space, even though f may not. K must also satisfy

$$\int_{\mathbb{R}^3} K^n(\boldsymbol{x}) \, \mathrm{d}V = 1, \qquad \forall \, n \in \mathbb{N} \tag{B.2}$$

where $K^n(\boldsymbol{x}) := (K * \ldots * K)(\boldsymbol{x})$ is the $(n-1)$-th convolution of the kernel with itself. Additionally, let ξ be the width of the kernel,

$$\xi^2 := \int_{\mathbb{R}^3} |\boldsymbol{x}|^2 K(\boldsymbol{x}) \, \mathrm{d}V, \tag{B.3}$$

such that K tends to the Dirac delta function, $K(\boldsymbol{x}) \to \delta(\boldsymbol{x})$, as $\xi \to 0$.

Let $\alpha_i : \mathbb{R}^3 \to [0, 1]$ be the volume fraction of phase i defined for all points in space. Then, assume that α_i changes sharply from 0 to 1 at $\boldsymbol{x}_s$ such that $S_i(\boldsymbol{x}_s) = \text{const.}$ corresponds to the two-dimensional manifold where the discontinuity of α_i occurs. Note that the discrete volume fractions in the VoF method can be constructed by $\tilde{\alpha}_i = K * \alpha_i$ for some K that averages the volume of phase i in every grid cell. As shown by Brackbill et al. [45],

$$\nabla \tilde{\alpha}_i = \oint_{\partial \Omega_i} K(\boldsymbol{x} - \boldsymbol{x}'_s) \, \mathrm{d}\boldsymbol{\sigma}(\boldsymbol{x}'_s), \tag{B.4}$$

where $\Omega_i = \{ \boldsymbol{x} : \alpha_i(\boldsymbol{x}) = 1 \}$ is the set of points occupied by phase i, $\partial \Omega_i$ is the boundary of Ω_i, and $\mathrm{d}\boldsymbol{\sigma}$ corresponds to the infinitesimal area element orthogonal to the surface and pointing into phase i. Then, $\nabla \tilde{\alpha}_i$ can be regarded as a continuation of the normal vector to the boundary of Ω_i.

It can be shown that the function $|\nabla \tilde{\alpha}_i|$ tends to the surface density function $\delta_i^{(S)}$ as ξ is reduced to 0. First, consider the integral,

$$\int_{\mathbb{R}^3} \left| \nabla \tilde{\alpha}_i \right| \mathrm{d}V = \int_{\mathbb{R}^3} \left| \oint_{\partial \Omega_i} K(\boldsymbol{x} - \boldsymbol{x}'_s) \, \mathrm{d}\boldsymbol{\sigma}(\boldsymbol{x}'_s) \right| \mathrm{d}V \leq \int_{\mathbb{R}^3} \oint_{\partial \Omega_i} K(\boldsymbol{x} - \boldsymbol{x}'_s) \left| \mathrm{d}\boldsymbol{\sigma}(\boldsymbol{x}'_s) \right| \mathrm{d}V \tag{B.5}$$

$$= \oint_{\partial \Omega_i} \int_{\mathbb{R}^3} K(\boldsymbol{x} - \boldsymbol{x}'_s) \, \mathrm{d}V \left| \mathrm{d}\boldsymbol{\sigma}(\boldsymbol{x}'_s) \right| = \oint_{\partial \Omega_i} |\, \mathrm{d}\boldsymbol{\sigma}'| = |\partial \Omega_i| \tag{B.6}$$

where, $|\partial \Omega_i|$ indicate the measure of the set $\partial \Omega_i$. For the last equality, the order of integration was swapped, and Eq. (B.2) was used. As $\xi \to 0$, i.e., $K \to \delta$, the first equality in Eq. (B.5) becomes

$$\lim_{\xi \to 0} \int_{\mathbb{R}^3} \left| \nabla \tilde{\alpha}_i \right| \mathrm{d}V = \int_{\mathbb{R}^3} \left| \oint_{\partial \Omega_i} \delta(\boldsymbol{x} - \boldsymbol{x}'_s) \, \mathrm{d}\boldsymbol{\sigma}(\boldsymbol{x}'_s) \right| \mathrm{d}V = |\partial \Omega_i|. \tag{B.7}$$

Consider the vector field

$$\boldsymbol{m}_{ik} := \alpha_k \nabla \tilde{\alpha}_i - \alpha_i \nabla \tilde{\alpha}_k \tag{B.8}$$

which can be regarded as a continuation of the gradient from phases k to i at their shared interface. Then, in a similar way, the function $|\boldsymbol{m}_{ik}|$ approaches the surface density function of the ik-interface,

$$\int_{\mathbb{R}^3} |\boldsymbol{m}_{ik}|\,\mathrm{d}V = \int_{\mathbb{R}^3} \left| \oint_{\partial\Omega_i} \alpha_k(\boldsymbol{x}) K(\boldsymbol{x}-\boldsymbol{x}'_s)\,\mathrm{d}\boldsymbol{\sigma}_i(\boldsymbol{x}'_s) - \oint_{\partial\Omega_k} \alpha_i(\boldsymbol{x}) K(\boldsymbol{x}-\boldsymbol{x}'_s)\,\mathrm{d}\boldsymbol{\sigma}_k(\boldsymbol{x}'_s) \right| \mathrm{d}V \tag{B.9}$$

$$= \int_{\Omega_i\cup\Omega_k} \left| \int_{\partial\Omega_i\cap\partial\Omega_k} K(\boldsymbol{x}-\boldsymbol{x}'_s)\,\mathrm{d}\boldsymbol{\sigma}_i(\boldsymbol{x}'_s) \right| \mathrm{d}V \leq \int_{\partial\Omega_i\cap\partial\Omega_k} |\,\mathrm{d}\boldsymbol{\sigma}| = |\partial\Omega_i\cap\partial\Omega_k|. \tag{B.10}$$

For the first equality, we have considered that $\alpha_i + \alpha_k = 1$ over the volume $\Omega_i \cup \Omega_k$ and zero otherwise, which follows from Eq. (1). Additionally, at the shared boundary of phases i and k, the normal vector to the surface points in opposite directions, i.e., $\mathrm{d}\boldsymbol{\sigma}_i(\boldsymbol{x}) + \mathrm{d}\boldsymbol{\sigma}_k(\boldsymbol{x}) = 0$ for $\boldsymbol{x} \in \partial\Omega_i \cap \partial\Omega_k$. The subindices, in this case, are placed to make explicit in which direction of the surface elements are pointing in. The equality holds for the limiting case in which the width of the convolution kernel goes to zero. Note that, in general, the surface $\partial\Omega_i \cap \partial\Omega_k$ is not closed and, therefore, has a finite perimeter.

The line density function can be constructed in the following way. Consider the vector field $\boldsymbol{m}$ defined by

$$\boldsymbol{m}(\boldsymbol{x}) := \int_{\Sigma} K(\boldsymbol{x}-\boldsymbol{x}'_s)\,\mathrm{d}\boldsymbol{\sigma}(\boldsymbol{x}'_s) \tag{B.11}$$

over some open surface Σ and local vector surface element, $\mathrm{d}\boldsymbol{\sigma}$. Then,

$$\nabla\times\boldsymbol{m} = \nabla\times\int_{\Sigma} K(\boldsymbol{x}-\boldsymbol{x}'_s)\,\mathrm{d}\boldsymbol{\sigma}(\boldsymbol{x}'_s) = \int_{\Sigma} \mathrm{d}\boldsymbol{\sigma}(\boldsymbol{x}'_s)\times\nabla K(\boldsymbol{x}-\boldsymbol{x}'_s) \tag{B.12}$$

$$= \oint_{\partial\Sigma} K(\boldsymbol{x}-\boldsymbol{x}'_l)\,\mathrm{d}\boldsymbol{\lambda}(\boldsymbol{x}'_l), \tag{B.13}$$

where $\partial\Sigma$ is the bounding perimeter of the surface Σ and $\mathrm{d}\boldsymbol{\lambda}$ is the infinitesimal line segment vector and $\boldsymbol{x}_l \in \partial\Sigma$ is the local position of the perimeter. In the last equality of Eq. (B.13), Stokes' theorem has been used. Note that, as the convolution kernel is narrowed down, $\nabla\times\boldsymbol{m}$ becomes parallel to the unit tangent vector of the surface perimeter. Consequently, the magnitude of the vector tends to the line density function,

$$\int_{\mathbb{R}^3} |\nabla\times\boldsymbol{m}|\,\mathrm{d}V = \int_{\mathbb{R}^3} \left| \oint_{\partial\Sigma} K(\boldsymbol{x}-\boldsymbol{x}'_l)\,\mathrm{d}\boldsymbol{\lambda}(\boldsymbol{x}'_l) \right| \mathrm{d}V \leq \int_{\mathbb{R}^3} \oint_{\partial\Sigma} K(\boldsymbol{x}-\boldsymbol{x}'_l) \left|\mathrm{d}\boldsymbol{\lambda}(\boldsymbol{x}'_l)\right| \tag{B.14}$$

$$= \oint_{\partial\Sigma} \int_{\mathbb{R}^3} K(\boldsymbol{x}-\boldsymbol{x}'_l)\,\mathrm{d}V \left|\mathrm{d}\boldsymbol{\lambda}(\boldsymbol{x}'_l)\right| = |\partial\Sigma|. \tag{B.15}$$

Furthermore, the equality holds when K is narrowed to the Dirac delta function.

In a similar way, the vector field $\nabla\times\boldsymbol{m}_{ik}$, as presented in Eq. (A.9), can now be expressed as

$$\nabla\times\boldsymbol{m}_{ik} = 2\nabla\tilde{\alpha}_k\times\nabla\tilde{\alpha}_i \approx \hat{\boldsymbol{b}}_{ik}\delta_{ik}^{(L)}, \tag{B.16}$$

where $\hat{\boldsymbol{b}}_{ik}$ is the extension of the unit tangent vector for the vicinity of the perimeter of the ik-interface and $\delta_{ik}^{(L)}$ its line density function. Consequently, the volume integral of the magnitude of the vector field in Eq. (B.16) results in the perimeter of the ik-interface,

$$\int_{\mathbb{R}^3} \left|\nabla\times\boldsymbol{m}_{ik}\right| \mathrm{d}V \approx |\partial(\partial\Omega_i\cap\partial\Omega_k)|. \tag{B.17}$$

Naturally, the equality of both Eqs. (B.16) and (B.17) is achieved in the limit $\xi \to 0$.

Appendix C. A preliminary algorithm for the triple line forces based on the Height Function (HF) method

In the Height Function (HF) method, the local profile of the ik-interface is obtained by constructing a function $H : \mathbb{Z}^{d-1} \to \mathbb{R}$, where d is the dimension of the system. H is obtained by carrying out a column summation of the volume fractions over a small vicinity of an interface [57,65,66]. For the preliminary algorithm proposed here, let H be defined as

$$H(m) := \sum_{l=-3}^{3} \frac{1}{2}\left[1 + \alpha_i(\boldsymbol{x}_{m'+m,n'+l}) - \alpha_k(\boldsymbol{x}_{m'+m,n'+l})\right], \quad m', n' \in \mathbb{Z} \text{ and } m = -1, 0, 1 \tag{C.1}$$

for the ik-interface in two-dimensions ($d = 2$) and inside a 3×7 neighbourhood of the point $\boldsymbol{x}_{m',n'}$ [66]. Eq. (C.1) performs an average of the distance from the i and k interface in the y direction. However, for the x direction, the summation is done about the index n'. In this case, the curvature is computed by

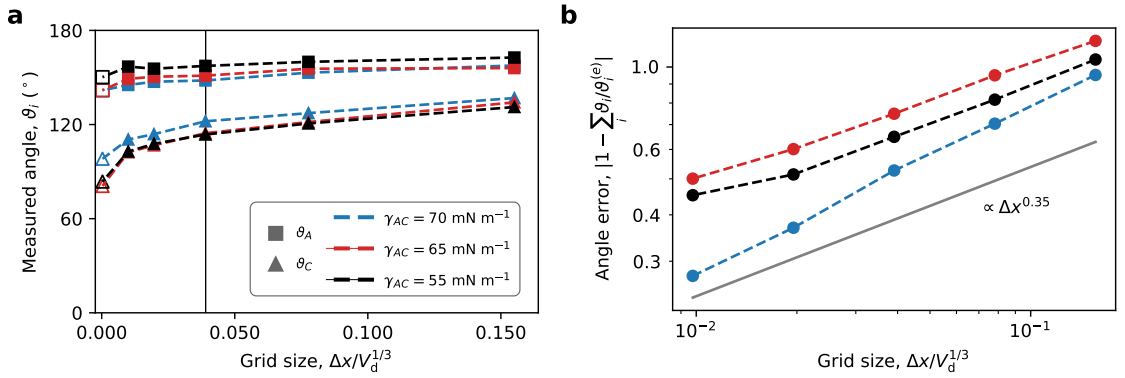

Fig. D.10. Convergence test for the liquid lentil setup. (a) Measured angles ϑ_A and ϑ_C after changing the grid resolution Δx. Δx is compared to the cubic root of the volume of the droplet, $V_d^{1/3}$, the latter setting the length scale of the system. The vertical line corresponds to the grid size for the simulations presented in Fig. 4. The empty markers, representing the limit of $\Delta x \to 0$ correspond to the expected value. (b) Relative error in the measured angle with respect to the expected angle for different grid sizes. The grey line shows the average exponent of the power-law trends. The surface tension constants are summarised in the legend of the panel a and all other simulation parameters are given in Fig. 4. (Colour online)

$$\kappa_{ik} \approx \frac{H(-1) - 2H(0) + H(1)}{\Delta x^2 \left[1 + (H(1) - H(-1))^2 \Delta x^{-2}/4\right]^{3/2}}, \tag{C.2}$$

which is derived from the curvature expression $\kappa = h''/(1 + h'^2)^{3/2}$ for some smooth curve h and then approximated by a three-point finite difference stencil. Additionally, the unit normal vector is redirected using H,

$$\hat{\boldsymbol{n}}_{ik}(\boldsymbol{x}_{m,n}) = \frac{1}{\sqrt{\Delta x^2 + (H(1) - H(-1))^2}} \begin{pmatrix} H(1) - H(-1) \\ -\Delta x \end{pmatrix}. \tag{C.3}$$

The forces at the triple line are calculated in a similar way. As in the previous approach, the line density function is calculated directly based on the volume fractions by taking the magnitude of Eq. (16),

$$\delta_{ik}^{(L)} := 2|\boldsymbol{\nabla}\alpha_k \times \boldsymbol{\nabla}\alpha_i|. \tag{C.4}$$

Then, the tangent vector to the ik-interface, $\hat{\boldsymbol{t}}_{ik}$, is corrected by means of a two-point stencil of H,

$$\hat{\boldsymbol{t}}_{ik}(\boldsymbol{x}_{m-1,n}) = \frac{1}{\sqrt{\Delta x^2 + (H(1) - H(0))^2}} \begin{pmatrix} \Delta x \\ H(1) - H(0) \end{pmatrix} \tag{C.5}$$

where it is assumed that the triple line is located inside the cell centred at $\boldsymbol{x}_{m-1,n}$. Note that the tangent vector evaluated at $\boldsymbol{x}_{m-1,n}$ is calculated one cell away in the direction of the ik-interface; this is done because the slope of the surface is ill-defined at the triple line since it corresponds to a wedge between the converging interfaces. Higher-order corrections to $\hat{\boldsymbol{t}}_{ik}$ can be implemented utilising a larger stencil or by transporting the unitary vector using detailed knowledge of the geometry of the interface.

Appendix D. Grid convergence assessment for the fluid-fluid contact angles

In addition to calculating the contact angles for the fluid-on-fluid system, the convergence of the force scheme for different grid resolutions is assessed; Fig. D.10 presents these results. To assess the convergence of the numerical method, we have employed the slope method to measure the contact angles between phases.

The slope method consists of measuring the contact angle by the slope that adjacent interfaces have at the triple line. This slope is calculated by pivoting about the triple line against the position of the interface at the neighbouring sites. Therefore, the slope method utilises only local information in the same way that the underlying numerical method calculates the surface tension forces. For that reason, the convergence of the measuring method is consistent with the numerical method.

Fig. D.10a shows the measured contact angle and the expected angle of the fluid-fluid triple line. It can be observed that, as the grid size is reduced, the measured angle decreases and approaches its expected value. In Fig. D.10b, the error in the measurement of the contact angle was calculated. It was found that the error is reduced by the grid size, Δx, as $O(\Delta x^{0.35})$, on average. This improvement is consistent with smoothing the volume fraction due to the numerical diffusivity that occurs due to the advection scheme in the algebraic VoF. By using a relatively small compression coefficient, $c_\alpha = 0.5$, the interface is naturally smoothed out, and the finite volume stencils have an improved convergence compared to a high compression coefficient.

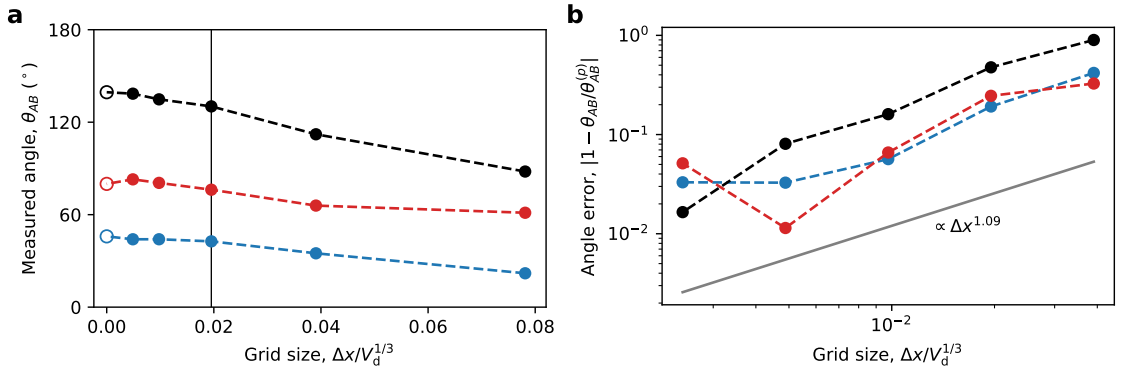

Fig. E.11. Convergence test for the sessile droplet case using the geometric approach to prescribe the wettability of the surface. (a) The measured contact angle, θ_{AB}, for different grid sizes, Δx. The grid size is compared to $V_d^{1/3}$ to set the system's length scale. The vertical line in the plots corresponds to the grid size for the simulations presented in Fig. 5. The prescribe value of the contact angle, representing the limit $\Delta x \to 0$, is indicated by the empty symbols. (b) Relative error in the measurement of the contact angle with respect to its prescribed value as shown in Figs. 5(c) and 5(d). The grey line in the panels indicates the average power-law exponent. (Colour online)

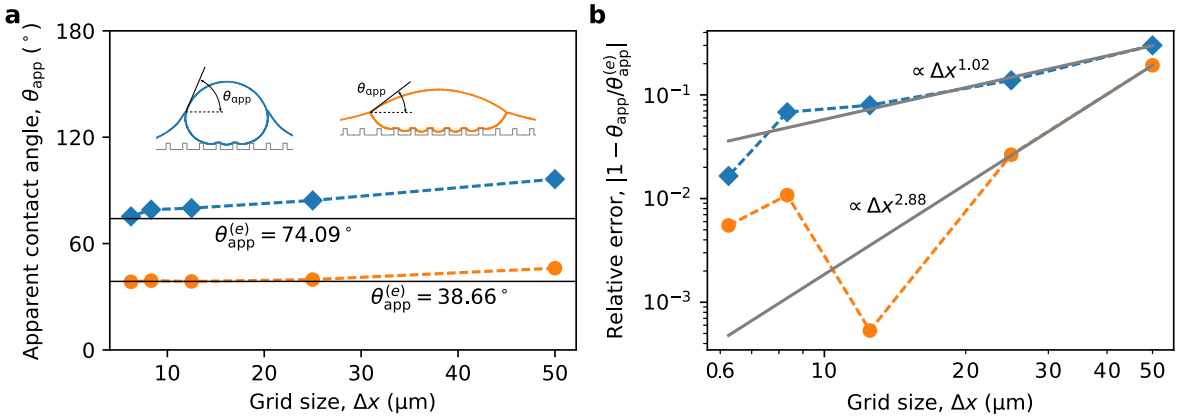

Fig. F.12. Convergence test for the FC70 and decanol LIS. These simulations correspond to the systems in Figs. 7a and 7c for different grid sizes. a) Measurement of the apparent contact angle for the FC70- and decanol-libricated LIS. The black lines correspond to the expected value, $\theta_{app}^{(e)}$, based on Richardson's extrapolation as $\Delta x \to 0$. b) Relative error and trend in the measurement of the apparent contact angle compared to the expected value. The grey lines show the trend of the power-law exponent. (Colour online)

Appendix E. Grid convergence assessment for the fluid-solid contact angles

Fig. E.11 shows the behaviour of the liquid-solid contact angle for varying grid size. As in Fig. D.10, the contact angles are calculated by the slope method, in which the intersection angle of the local slope of the interface is measured against the solid surface.

Fig. E.11(a) shows how the accuracy in the contact angle improves as the grid is refined. Fig. E.11(b) shows the error in the measurement of the fluid-solid contact angle against the prescribed one by the geometric approach, $\theta_{AB}^{(p)}$. It can be observed that the contact angle converges at a rate of $\sim \Delta x^{1.09}$, approximately. As discussed before, this improvement can be associated to the effect of smoothing the volume fraction due to the numerical diffusivity by using a relatively small compression coefficient, $c_\alpha = 0.5$.

Appendix F. Grid convergence assessment on LIS

The equilibrium configuration state of the two LIS shown in Fig. 7 is compared in Fig. F.12. Here, the apparent contact angle, θ_{app}, is measured for different grid sizes. The apparent contact angle is a relevant quantity in the characterisation of the LIS. Formally, it is defined as the angle that the spherical cap of the droplet draws against the plane parallel to the surface as shown in the insets of Fig. F.12a. The apparent contact angle depends on the height of the meniscus and the Neumann triangle formed by the interfaces. Therefore, θ_{app} depends on the surface tensions of the three fluid phases, and on the relative pressure differences of the meniscus and the droplet [67].

In Fig. F.12a the apparent contact angle is calculated for the FC70- and decanol-lubricated surfaces. It can be observed that the apparent contact angle converges to $\theta_{app}^{(e)} = 74.09°$ and $\theta_{app}^{(e)} = 38.66°$, respectively. Here, $\theta_{app}^{(e)}$ was obtained by employing the Richardson extrapolation method [68]. Taking the asymptotic value, the relative error is reported in Fig. F.12b. It can be observed that, on average, the convergence to the extrapolated angle is higher than $O(\Delta x)$ for both FC70- and decanol-lubricated LIS, respectively.

References

[1] U. Hecht, L. Gránásy, T. Pusztai, B. Böttger, M. Apel, V. Witusiewicz, L. Ratke, J. De Wilde, L. Froyen, D. Camel, B. Drevet, G. Faivre, S. Fries, B. Legendre, S. Rex, Multiphase solidification in multicomponent alloys, Mater. Sci. Eng., R Rep. 46 (2004) 1–49.
[2] I. Steinbach, Phase-field models in materials science, Model. Simul. Mater. Sci. Eng. 17 (2009) 073001.
[3] E.D. Wilde, I. Bellemans, M. Campforts, A. Khaliq, K. Vanmeensel, D. Seveno, M. Guo, A. Rhamdhani, G. Brooks, B. Blanpain, N. Moelans, K. Verbeken, Wetting behaviour of Cu based alloys on spinel substrates in pyrometallurgical context, Mater. Sci. Technol. 31 (2015) 1925–1933.
[4] V.I. Levitas, A.M. Roy, Multiphase phase field theory for temperature-induced phase transformations: formulation and application to interfacial phases, Acta Mater. 105 (2016) 244–257.
[5] S.I. Abo-El Ela, S.S. Nawar, Treatment of wastewater from an oil and soap factory via dissolved air flotation, Environ. Int. 4 (1980) 47–52.
[6] R. Moosai, R.A. Dawe, Gas attachment of oil droplets for gas flotation for oily wastewater cleanup, Sep. Purif. Technol. 33 (2003) 303–314.
[7] L. Zeng, D. Velez, J. Lu, G. Tryggvason, Numerical studies of disperse three-phase fluid flows, Fluids 6 (2021).
[8] G. Brenn, Droplet Collision, Springer, 2011.
[9] Y. Yeo, A.U. Chen, O.A. Basaran, K. Park, Solvent exchange method: a novel microencapsulation technique using dual microdispensers, Pharm. Res. 21 (2004) 1419–1427.
[10] M. Windbergs, Y. Zhao, J. Heyman, D.A. Weitz, Biodegradable core–shell carriers for simultaneous encapsulation of synergistic actives, J. Am. Chem. Soc. 135 (2013) 7933–7937.
[11] A.W. Adamson, A.P. Gast, et al., Physical Chemistry of Surfaces, vol. 150, Interscience Publishers, New York, 1967.
[12] J.D. Smith, R. Dhiman, S. Anand, E. Reza-Garduno, R.E. Cohen, G.H. McKinley, K.K. Varanasi, Droplet mobility on lubricant-impregnated surfaces, Soft Matter 9 (2013) 1772–1780.
[13] F. Schellenberger, J. Xie, N. Encinas, A. Hardy, M. Klapper, P. Papadopoulos, H.-J. Butt, D. Vollmer, Direct observation of drops on slippery lubricant-infused surfaces, Soft Matter 11 (2015) 7617–7626.
[14] D. Daniel, J.V.I. Timonen, R. Li, S.J. Velling, J. Aizenberg, Oleoplaning droplets on lubricated surfaces, Nat. Phys. 13 (2017) 1020–1025.
[15] J. Kim, Phase-field models for multi-component fluid flows, Commun. Comput. Phys. 12 (2012) 613–661.
[16] S. Dong, An efficient algorithm for incompressible N-phase flows, J. Comput. Phys. 276 (2014) 691–728.
[17] G.I. Tóth, M. Zarifi, B. Kvamme, Phase-field theory of multicomponent incompressible Cahn-Hilliard liquids, Phys. Rev. E 93 (2016) 013126.
[18] S. Ciro, T. Krüger, H. Kusumaatmaja, Ternary free-energy lattice Boltzmann model with tunable surface tensions and contact angles, Phys. Rev. E 93 (2016) 033305.
[19] Z. Huang, G. Lin, A.M. Ardekani, A consistent and conservative model and its scheme for N-phase-M-component incompressible flows, J. Comput. Phys. 434 (2021) 110229.
[20] S. Mirjalili, C.B. Ivey, A. Mani, Comparison between the diffuse interface and volume of fluid methods for simulating two-phase flows, Int. J. Multiph. Flow 116 (2019) 221–238.
[21] S. Dong, Multiphase flows of n immiscible incompressible fluids: a reduction-consistent and thermodynamically-consistent formulation and associated algorithm, J. Comput. Phys. 361 (2018) 1–49.
[22] R. Haghani Hassan Abadi, M.H. Rahimian, A. Fakhari, Conservative phase-field lattice-boltzmann model for ternary fluids, J. Comput. Phys. 374 (2018) 668–691.
[23] S. Mirjalili, A. Mani, A conservative second order phase field model for simulation of n-phase flows, J. Comput. Phys. 498 (2024) 112657.
[24] A. Prosperetti, G. Tryggvason, Computational Methods for Multiphase Flow, Cambridge University Press, 2007.
[25] F. Losasso, T. Shinar, A. Selle, R. Fedkiw, Multiple interacting liquids, ACM Trans. Graph. 25 (2006) 812–819.
[26] D.P. Starinshak, S. Karni, P.L. Roe, A new level-set model for multimaterial flows, J. Comput. Phys. 262 (2014) 1–16.
[27] H. Li, Y. Yap, J. Lou, Z. Shang, Numerical modelling of three-fluid flow using the level-set method, Chem. Eng. Sci. 126 (2015) 224–236.
[28] G. Tryggvason, R. Scardovelli, S. Zaleski, Direct Numerical Simulations of Gas–Liquid Multiphase Flows, Cambridge University Press, 2011.
[29] A.A. Howard, A.M. Tartakovsky, A conservative level set method for N-phase flows with a free-energy-based surface tension model, J. Comput. Phys. 426 (2021) 109955.
[30] R. Scardovelli, S. Zaleski, Direct numerical simulation of free-surface and interfacial flow, Annu. Rev. Fluid Mech. 31 (1999) 567–603.
[31] B. Lafaurie, C. Nardone, R. Scardovelli, S. Zaleski, G. Zanetti, Modelling merging and fragmentation in multiphase flows with surfer, J. Comput. Phys. 113 (1994) 134–147.
[32] S.P. Schofield, R.V. Garimella, M.M. Francois, R. Loubère, A second-order accurate material-order-independent interface reconstruction technique for multi-material flow simulations, J. Comput. Phys. 228 (2009) 731–745.
[33] B. Blais, J.-P. Braeunig, D. Chauveheid, J.-M. Ghidaglia, R. Loubère, Dealing with more than two materials in the FVCF–ENIP method, Eur. J. Mech. B, Fluids 42 (2013) 1–9.
[34] A. Pathak, M. Raessi, A three-dimensional Volume-of-Fluid method for reconstructing and advecting three-material interfaces forming contact lines, J. Comput. Phys. 307 (2016) 550–573.
[35] A.K. Pandare, J. Waltz, J. Bakosi, Multi-material hydrodynamics with algebraic sharp interface capturing, Comput. Fluids 215 (2021) 104804.
[36] R. Bonhomme, J. Magnaudet, F. Duval, B. Piar, Inertial dynamics of air bubbles crossing a horizontal fluid–fluid interface, J. Fluid Mech. 707 (2012) 405–443.
[37] P. Personnettaz, P. Beckstein, S. Landgraf, T. Köllner, M. Nimtz, N. Weber, T. Weier, Thermally driven convection in Li-Bi liquid metal batteries, J. Power Sources 401 (2018) 362–374.
[38] S. Bublik, K.E. Einarsrud, Inverse modelling of interfacial tension between ferroalloy and slag using OpenFOAM, in: 14th International Conference on CFD in 6 Oil & Gas, Metallurgical and Process Industries SINTEF, Trondheim, Norway, October 12–14, SINTEF Academic Press, 2020, pp. 12–14, 2020.
[39] F. Boyer, C. Lapuerta, Study of a three component Cahn-Hilliard flow model, ESAIM: M2AN 40 (2006) 653–687.
[40] H. Liang, B.C. Shi, Z.H. Chai, Lattice Boltzmann modeling of three-phase incompressible flows, Phys. Rev. E 93 (2016) 013308.
[41] H. Liang, J. Xu, J. Chen, Z. Chai, B. Shi, Lattice Boltzmann modeling of wall-bounded ternary fluid flows, Appl. Math. Model. 73 (2019) 487–513.
[42] C. Dritselis, G. Karapetsas, Open-source finite volume solvers for multiphase (N-phase) flows involving either Newtonian or non-Newtonian complex fluids, Comput. Fluids 245 (2022) 105590.
[43] C. Bilger, M. Aboukhedr, K. Vogiatzaki, R. Cant, Evaluation of two-phase flow solvers using level set and volume of fluid methods, J. Comput. Phys. 345 (2017) 665–686.
[44] J. Roenby, H. Bredmose, H. Jasak, IsoAdvector: Geometric VOF on General Meshes, Springer International Publishing, Cham, 2019, pp. 281–296.
[45] J. Brackbill, D. Kothe, C. Zemach, A continuum method for modeling surface tension, J. Comput. Phys. 100 (1992) 335–354.
[46] M. Spivak, A Comprehensive Introduction to Differential Geometry, vol. 2, Publish or Perish, 1979.
[47] P.-G. de Gennes, F. Brochard-Wyart, D. Quéré, Capillarity and Wetting Phenomena: Drops, Bubbles, Pearls, Waves, Springer Science & Business Media, 2013.
[48] A. Marchand, S. Das, J.H. Snoeijer, B. Andreotti, Contact angles on a soft solid: from Young's law to Neumann's law, Phys. Rev. Lett. 109 (2012) 236101.
[49] S. Pope, The evolution of surfaces in turbulence, Int. J. Eng. Sci. 26 (1988) 445–469.
[50] C. Pozrikidis, Boundary Integral and Singularity Methods for Linearized Viscous Flow, Cambridge University Press, 1992.
[51] J.A. Heyns, A.G. Malan, T.M. Harms, O.F. Oxtoby, Development of a compressive surface capturing formulation for modelling free-surface flow by using the volume-of-fluid approach, Int. J. Numer. Methods Fluids 71 (2013) 788–804.

[52] H. Ding, P.D.M. Spelt, Wetting condition in diffuse interface simulations of contact line motion, Phys. Rev. E 75 (2007) 046708.
[53] H.G. Weller, G. Tabor, H. Jasak, C. Fureby, A tensorial approach to computational continuum mechanics using object-oriented techniques, Comput. Phys. 12 (1998) 620–631.
[54] B. van Leer, Towards the ultimate conservative difference scheme. II. Monotonicity and conservation combined in a second-order scheme, J. Comput. Phys. 14 (1974) 361–370.
[55] N. Bala, M. Pepona, I. Karlin, H. Kusumaatmaja, C. Semprebon, Wetting boundaries for a ternary high-density-ratio lattice-Boltzmann method, Phys. Rev. E 100 (2019) 013308.
[56] L.A. Girifalco, R.J. Good, A theory for the estimation of surface and interfacial energies. I. Derivation and application to interfacial tension, J. Phys. Chem. C 61 (1957) 904–909.
[57] F. Evrard, F. Denner, B. van Wachem, Height-function curvature estimation with arbitrary order on non-uniform cartesian grids, J. Comput. Phys. X 7 (2020) 100060.
[58] P. Cifani, W. Michalek, G. Priems, J. Kuerten, C. van der Geld, B. Geurts, A comparison between the surface compression method and an interface reconstruction method for the VOF approach, Comput. Fluids 136 (2016) 421–435.
[59] M. Sussman, M. Ohta, High-order techniques for calculating surface tension forces, in: I.N. Figueiredo, J.F. Rodrigues, L. Santos (Eds.), Free Boundary Problems, Birkhäuser Basel, Basel, 2007, pp. 425–434.
[60] S. Popinet, Numerical models of surface tension, Annu. Rev. Fluid Mech. 50 (2018) 49–75.
[61] M.D. Torrey, L.D. Cloutman, R.C. Mjolsness, C. Hirt, Nasa-vof2d: a computer program for incompressible flows with free surfaces, NASA STI/Recon Techn. Rep. N 86 (1985) 30116.
[62] J.S. Rowlinson, B. Widom, Molecular Theory of Capillarity, Courier Corporation, 2013.
[63] A.J.M. Yang, P.D. Fleming, J.H. Gibbs, Molecular theory of surface tension, J. Chem. Phys. 64 (1976) 3732–3747.
[64] R.C. Tolman, The superficial density of matter at a liquid-vapor boundary, J. Chem. Phys. 17 (1949) 118–127.
[65] S.J. Cummins, M.M. Francois, D.B. Kothe, Estimating curvature from volume fractions, in: Frontier of Multi-Phase Flow Analysis and Fluid-Structure, Comput. Struct. 83 (2005) 425–434.
[66] S. Popinet, An accurate adaptive solver for surface-tension-driven interfacial flows, J. Comput. Phys. 228 (2009) 5838–5866.
[67] C. Semprebon, G. McHale, H. Kusumaatmaja, Apparent contact angle and contact angle hysteresis on liquid infused surfaces, Soft Matter 13 (2017) 101–110.
[68] P. Moin, Fundamentals of Engineering Numerical Analysis, Cambridge University Press, 2010.